Two-channel quantum wire with an adatom impurity: Role of the van Hove singularity in the quasibound state in continuum, decay rate amplification, and the Fano effect

S. Garmon,[1,*] H. Nakamura,[2,†] N. Hatano,[3,‡] and T. Petrosky[4,§]
[1]*Niels Bohr Institute, Blegdamsvej 17, 2100 Copenhagen Ø, Denmark*
[2]*National Institute for Fusion Science, Oroshi-cho 322-6, Toki, Gifu 509-5292, Japan*
[3]*Institute of Industrial Science, University of Tokyo, Komaba 4-6-1, Meguro, Tokyo 153-8505, Japan*
[4]*Center for Complex Quantum Systems, University of Texas at Austin, 1 University Station, C1609, Austin, Texas 78712, USA*
(Received 11 August 2008; revised manuscript received 10 July 2009; published 18 September 2009)

We provide detailed analysis of the complex eigenenergy spectrum for a two-channel quantum wire with an attached adatom impurity. The study is based on our previous work [Phys. Rev. Lett. **99**, 210404 (2007)], in which we presented the quasibound states in continuum (or QBIC states). These are resonant states with very long lifetime that form as a result of two overlapping continuous energy bands, one of which, at least, has a divergent van Hove singularity at the band edge. We provide analysis of the full energy spectrum for all solutions, including the QBIC states, and obtain an expansion for the complex eigenvalue of the QBIC state. We show that it has a small decay rate of the order g^6, where g is the coupling constant of the adatom impurity. As a result of this expansion, we find that this state is a nonanalytic effect resulting from the van Hove singularity; it cannot be predicted from the ordinary perturbation analysis that relies on Fermi's golden rule. We also show that the QBIC state emerges as a direct result of the destabilization of the stable state that often exists on the outside edge of a band due to the divergence. As another result of the van Hove singularity, it has been previously reported that the decay rate of an unstable state is amplified in the vicinity of the band edge such that it is proportional to $g^{4/3}$. This again results from a breakdown of the Fermi rule. Here we explicitly show how the system behaves in the crossover region between the $g^{4/3}$ region and the Fermi region. Finally, we calculate the local density of states near the adatom. We are able to demonstrate that the interference between two unstable states with a very large decay rate and one unstable state with a small decay rate results in a characteristic asymmetric Fano profile. This effect leads to the best chance of detecting the QBIC by scanning tunneling microscopy probe.

DOI: 10.1103/PhysRevB.80.115318 PACS number(s): 73.21.Hb, 03.65.Ge, 73.20.At

I. INTRODUCTION

In a previous letter[1] we introduced the *quasibound states in continuum* (QBIC states) as resonant states which occur in certain systems with overlapping continuous energy bands. Consider the case where one of these energy bands has a divergent van Hove singularity in the density of states (DOS) at one of the overlapping band edges. Then a discrete excited state coupled to these energy bands gives rise to a metastable resonant state with an extended lifetime. Further, this metastable state has real part of the energy that lies in one of the bands. This effect cannot be predicted using Fermi's golden rule as it breaks down in the vicinity of the singularity.

In our paper, we demonstrated the existence of the QBIC states in the context of a two-channel quantum wire coupled to a single adatom impurity. This built on previous work by Tanaka *et al.* on a single-channel wire coupled to an adatom,[2] in which they demonstrated various nonanalytic effects that resulted from the presence of the divergent van Hove singularity in the electron DOS[3] at the edge of the conduction band; note that these are characteristic effects of the van Hove singularity in a one-dimensional system. One of these effects was a bound state that lies just outside of either edge of the conduction band no matter how deeply the discrete adatom energy is embedded in the band.[2,4–6] We will refer to this state here as a *persistent bound state* or persistent stable state as it coexists with the unstable decay states even though it might be expected to vanish in the case where no divergence is present. In the present paper, we will show that when the adatom is coupled to a second energy band that overlaps the first, this persistent bound state is slightly destabilized due to the fact that it lies in the continuum of the second energy band. We will explicitly demonstrate that it is this persistent bound state (when destabilized) that forms the QBIC eigenstate for the two-channel system; for this purpose, we compare term by term the analytic expansions of the bound state energy eigenvalue in the single-channel system and that of the QBIC energy eigenvalue in the two-channel system. We will also show that the decay rate for the QBIC state is (to the lowest order) proportional to g^6, where g is the coupling constant between the adatom and the site to which it is attached. We assume that g is small in this paper.

We have envisioned the QBIC state as a generalization of the bound state in continuum (BIC), originally proposed by von Neumann and Wigner in 1929.[7] Since their initial proposal, a good deal of theoretical study has been devoted to this phenomenon,[8–18] including a recent paper by Longhi, in which the author demonstrated the presence of BIC states in a single level semi-infinite Fano-Anderson model[19] and another article by Tanaka *et al.*, in which the authors demonstrated the presence of BIC states in a single-channel quantum wire coupled with multiple adatom impurities.[6,20] These two studies are connected by symmetry considerations.[21] There has also been experimental confirmation of the BIC phenomenon.[22,23] However, since it is a zero measure effect

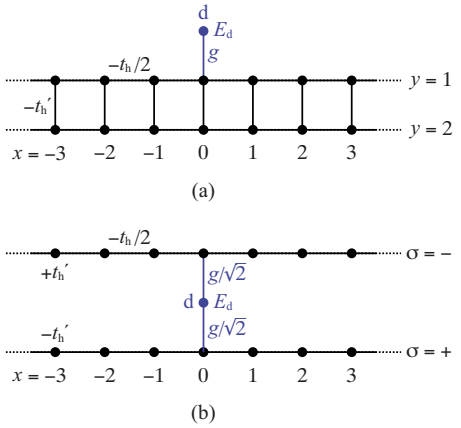

FIG. 1. (Color online) (a) An adatom (quantum dot) attached to a ladder. (b) After partial diagonalization in the y direction, the system is composed of the dot coupled to two independent channels.

(meaning that it only occurs at discrete points in parameter space), it is generally considered difficult to detect.

As discussed in our previous letter, the QBIC state actually has a decay rate (due to the imaginary part of the complex eigenenergy) and hence does not technically lie in the continuous energy spectrum of the conduction band. However, the decay rate for this state is on the order of g^6, much smaller than the ordinary decay rate that is predicted to be of the order g^2 by Fermi's golden rule. Hence the QBIC state will behave as a bound state (with real part of the complex energy inside the continuous energy spectrum) even on relatively large time scales. We will also show below that the g^6 power in the decay rate is a direct result of the interaction between the divergent van Hove singularity at one of the band edges and the continuum of the other band.

While the BIC states occur only at discrete parameter values, the QBIC states occur over a wide range of parameter space. Hence, it may be much easier to verify the QBIC effect experimentally. It may also be easier to verify the QBIC, considering that the effect will likely occur in physical systems other than the two-channel nanowire; we return to this point in the conclusion.

We also wish to clarify that the QBIC phenomenon is distinct from the BIC-like states that have been proposed in recent years by Rotter and Sadreev.[17,18] While the characteristics of the two types of states are similar (resonant state in the continuum with narrow width), the physical origin of each is quite different. Since the ordinary BIC states may arise due to symmetry (this can be viewed as a diffraction effect[2]), introducing a small spatial distortion into the Hamiltonian leads to a slight destabilization of the BIC, which is the origin of the BIC-like state as defined in Ref. 18. Hence the BIC-like states are associated with a spatial distortion in a single channel, while the QBIC state is associated with an embedded DOS singularity in a system with multiple channels.

For the present case, we consider the system shown in Fig. 1(a), which is composed of two tight-binding chains and an adatom or quantum dot impurity. The two tight-binding chains [labeled $y=1,2$ in Fig. 1(a)] both have internal hopping parameter $-t_h/2$ (internal sites of both chains are labeled by integer x, where $|x| \leq m$ with $N=2m+1$ and N ($\gg 1$) is the number of sites in either chain, $y=1$ or 2). The two chains are then coupled together site by site with hopping parameter $-t_h'$, creating a ladder shape. The dot (labeled d) is coupled to the $x=0$ site of the $y=1$ chain with the coupling constant g. Hence, we can write the Hamiltonian for our system as

$$\hat{\mathcal{H}} = -\frac{t_h}{2}\sum_{y=1,2}\sum_{x}(|x+1,y\rangle\langle x,y| + |x,y\rangle\langle x+1,y|) - t_h'\sum_{x}(|x,1\rangle \times \langle x,2| + |x,2\rangle\langle x,1|) + g(|d\rangle\langle 0,1| + |0,1\rangle\langle d|) + E_d|d\rangle\langle d|, \tag{1}$$

in which E_d denotes the energy of the dot. In accordance with our designations in Fig. 1, the first term here represents internal hopping along either of the chains (in the x direction) while the second term describes hopping from one chain to the other ($y=1$ to $y=2$ and vice versa). The third term then represents hopping between the adatom and the (0,1) site of the ladder and finally the fourth term gives the unperturbed energy of the adatom for $g=0$.

In order to diagonalize the second term of Hamiltonian (1), we introduce the basis

$$\begin{pmatrix} |x,+\rangle \\ |x,-\rangle \end{pmatrix} \equiv U \begin{pmatrix} |x,1\rangle \\ |x,2\rangle \end{pmatrix}, \tag{2}$$

where

$$U \equiv \frac{1}{\sqrt{2}}\begin{pmatrix} 1 & 1 \\ 1 & -1 \end{pmatrix} = U^{-1}. \tag{3}$$

Using the new basis $|x,\sigma=\pm\rangle$, the Hamiltonian can be divided into the $\sigma=+$ and $-$ chains (with the adatom term) as

$$\hat{\mathcal{H}} = \sum_{\sigma=\pm}\left[-\frac{t_h}{2}\sum_{x}(|x+1,\sigma\rangle\langle x,\sigma| + |x,\sigma\rangle\langle x+1,\sigma|) - \sigma t_h'\sum_{x}|x,\sigma\rangle\langle x,\sigma| + \frac{g}{\sqrt{2}}(|d\rangle\langle 0,\sigma| + |0,\sigma\rangle\langle d|)\right] + E_d|d\rangle\langle d|. \tag{4}$$

We have now obtained the Hamiltonian in the form of Fig. 1(b), in which the two $\sigma=+,-$ chains represent two independent channels for charge transfer. Note that we can also interpret the label σ as electron spin and t_h' as a magnetic field. In this case, the adatom term would act as a magnetic impurity similar to that in the Kondo model.[24,25]

In Sec. II, we will outline two approaches to obtaining the full diagonalization of the above Hamiltonian. In the first approach, we will introduce the wave vector representation to obtain a Friedrichs-type form of the Hamiltonian, from which we can obtain the energy eigenvalues of the system following the analysis due to Friedrichs.[26] In the second approach we will rely on the recently presented method of outgoing waves.[27]

In Sec. III we will present the full energy eigenvalue spectrum for the case in which the energy bands associated with the two channels of the quantum wire overlap; we show the

energy shift and decay rate of the QBIC states. In particular, we will show that the decay rate of the QBIC states is proportional to g^6 and that this effect is a direct result of the interaction between the van Hove singularity at the edge of one energy band and the continuum of the other energy band. We will then examine the wave function and time evolution and determine the spectral weight for the QBIC state. While we will find that the spectral weight for the QBIC is small in comparison to the ordinary Fermi-like resonant state with decay rate $\sim g^2$, the expression for the spectral weight will lead us to an intermediate type of QBIC state with reduced metastability (decay rate $g^6 < \gamma < g^2$) but significantly enhanced spectral weight. We refer to this state as an emerging QBIC.

In Sec. IV we will examine the role of the van Hove singularity in two other interesting physical effects. In the first case we will examine more closely the $g^{4/3}$ decay behavior that dominates the energy spectrum when the impurity energy lies near any of the band-edge singularities, as presented in earlier studies.[2,5] We will show explicitly how the system crosses over from the region where Fermi's golden rule holds (decay rate $\sim g^2$) to the region where the decay rate is amplified by the singularity (decay rate $\sim g^{4/3}$). In the second case we will calculate the local density of states (LDOS) function near the adatom site. In the vicinity of the van Hove singularity, we will find that the presence of two unstable states with decay rate $\sim g^{4/3}$ amplified by the singularity and another unstable state with smaller decay rate $\sim g^2$ will give rise to a specific type of Fano asymmetry in the LDOS profile, as predicted in Refs. 28 and 29. Finally, we will study this Fano effect in the case where the impurity energy lies close to the embedded band edge such that the emerging QBIC mentioned above is present. We will find that the presence of this state in the LDOS profile is amplified by the Fano interference. Hence, this yields the best chances of experimental detection of the QBIC by scanning tunneling microscopy (STM) probe.

In Sec. V we will examine the energy spectrum in two special cases. In the first case the two channels become decoupled when $t_h' = 0$. The energy spectrum then reduces to that of a single-channel quantum wire coupled with an adatom.[2] In the second case the lower edge of the upper band coincides with the upper edge of the lower band (that is, $t_h' = t_h$). We will then examine the energy spectrum and discover a modification of the QBIC states resulting from the two overlapping singularities. Finally, we will examine how the QBIC decay rate behaves in crossing over from the ordinary case ($\sim g^6$) to the modified case ($\sim g^4$).

Finally, in Sec. VI we will briefly outline our results and make our final conclusions. In the Appendix, we summarize our method for obtaining the numerical simulation for the time-evolution presented in Sec. III.

II. DISPERSION RELATION AND DIAGONALIZATION OF THE HAMILTONIAN

In this section we will outline two methods for diagonalizing Hamiltonian (4). In the first we will write the Hamiltonian in a Friedrichs form, from which we can immediately obtain the Green's function as well as the eigenvalues following the method due to Friedrichs.[26] These eigenvalues will be obtained in the form of discrete solutions to a dispersion relation that is equivalent to a 12th-order polynomial. The discrete solutions of this polynomial give the diagonalized energy shifts and decay rates for an electron in the adatom.

In the second approach we will rely on the method of outgoing waves presented recently by Hatano *et al.*[27] This method will also yield the dispersion relation, but it is better suited for performing numerical simulations.

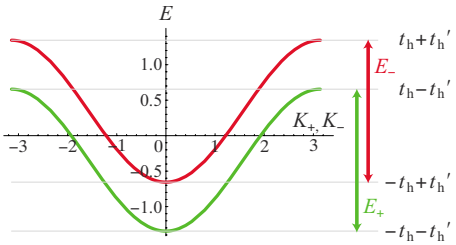

FIG. 2. (Color online) The two continuous dispersion relations [Eq. (7)] which form two conduction bands (channels) $E_\pm$ in the wire system. Here we graph the overlapping case in which $0 < t_h' < t_h$. Energy is measured in units of $t_h = 1$.

A. Dispersion relation from the Friedrichs solution

Imposing here the usual periodic boundary conditions in the x direction (as we are interested in the case $N \gg 1$), we may introduce the wave vector representation with wave vectors $K_\pm$ in the two respective channels $\sigma = \pm$ by

$$|K_\pm\rangle = \frac{1}{\sqrt{N}} \sum_x e^{iK_\pm x} |x, \pm\rangle, \tag{5}$$

where $K_\pm \equiv n_\pm \Delta k$ with $\Delta k \equiv 2\pi/N$ and integers $n_\pm$. This allows us to write Hamiltonian (4) as a variation in the Friedrichs-Fano model,

$$\hat{\mathcal{H}} = \sum_{\sigma=\pm} \sum_{K_\sigma} \left[E_\sigma |K_\sigma\rangle\langle K_\sigma| + \frac{g}{\sqrt{2N}} (|\mathrm{d}\rangle\langle K_\sigma| + |K_\sigma\rangle\langle \mathrm{d}|) \right] + E_\mathrm{d} |\mathrm{d}\rangle\langle \mathrm{d}|. \tag{6}$$

The energies E_σ in the two channels are determined by their respective wave numbers K_σ according to

$$E_\pm = -t_h \cos K_\pm \mp t_h'. \tag{7}$$

We refer to the above equations as the dispersion equations for the continua; this is because in the continuous limit $N \to \infty$ they describe the allowed energies for the two continua of K_σ states. In Fig. 2 we graph these two energy bands for the case $t_h' < t_h$, in which they will overlap. (By contrast, below we will write a discrete dispersion equation that describes how the discrete energy E_d is modified by the interaction.) Both of the continuous channels described in Eq. (7) have an associated DOS function. The normalized DOS functions for the two channels are given by

$$\rho_{\pm}(E) = \frac{1}{\pi\sqrt{t_h^2 - (E \pm t_h')^2}}. \tag{8}$$

Note the presence of two van Hove singularities in either channel. These singularities are located at $E = \pm t_h + t_h'$ for the "–" channel and $E = \pm t_h - t_h'$ for the "+" channel.

Since Hamiltonian (6) is in a Friedrichs-like form, in principle we may now diagonalize to solve the problem according to the method given by Friedrichs[26] that provides both the explicit eigenstates and the dispersion equation for the eigenvalues. In practice we may quickly find the eigenvalues as the poles of the Green's function for the adatom,

$$G_{dd}(z) \equiv \langle d|\frac{1}{z - \mathcal{H}}|d\rangle, \tag{9}$$

following the standard method.[30] The dispersion relation for the eigenvalues $\eta(z)=0$ is then obtained after we define $\eta(z)=[G_{dd}(z)]^{-1}$. Hence we will leave the details of obtaining the explicit solutions and the dispersion equation to Sec. II B, in which the method is more suited to conducting numerical simulations for the time evolution of the system.

The dispersion relation for the discrete adatom site is given by $\eta(z) \equiv z - E_d - \Xi_d(z) = 0$, where the self-energy $\Xi_d(z)$ for an electron embedded in the adatom is determined by

$$\begin{aligned}\Xi_d(z) &\equiv \frac{g^2}{2N}\sum_{\sigma=\pm}\sum_{k_\sigma}\frac{1}{z - E_{k_\sigma}} \\ &= \frac{g^2}{2N}\left[\sum_{k_+}\frac{1}{z + t_h' - t_h\cos k_+} + \sum_{k_-}\frac{1}{z - t_h' - t_h\cos k_-}\right] \\ &\overset{N\to\infty}{\to} \frac{g^2}{4\pi}\int_{-\pi}^{\pi} dk\left[\frac{1}{z + t_h' - t_h\cos k_+} + \frac{1}{z - t_h' - t_h\cos k_-}\right] \\ &= \frac{g^2}{2}\left[\frac{1}{\sqrt{(z + t_h')^2 - t_h^2}} + \frac{1}{\sqrt{(z - t_h')^2 - t_h^2}}\right].\end{aligned} \tag{10}$$

Thus we find the dispersion equation

$$z - E_d - \frac{g^2}{2}\left[\frac{1}{\sqrt{(z + t_h')^2 - t_h^2}} + \frac{1}{\sqrt{(z - t_h')^2 - t_h^2}}\right] = 0 \tag{11}$$

as reported previously.[1] From the one-particle perspective, this dispersion equation describes the behavior of an electron initially trapped in the adatom. By squaring twice, this equation can be written as a 12th-order polynomial equation in z. Hence, we will also refer to this equivalent equation as the *dispersion polynomial*. The 12 discrete solutions to this equation give the allowed bound states (purely real solutions) and resonant states (complex solutions) in the diagonalized system. As we will discuss below, these solutions can be viewed as living in a complex energy surface, parametrized by the original impurity energy E_d. In the present case of the two-channel wire, this energy surface will be composed of four Riemann sheets.

Once we have obtained the 12 discrete solutions $z=E$ to the dispersion polynomial, then Eq. (7) implies that each eigenvalue E can be assigned two $K_\pm$ values. With the values $K_\pm$ in hand, we will be able to write the wave function for each solution, making use of Eq. (13) given below. Practically, this means that any electron state in the wire can be fully described by the three values E, K_+, and K_-.

B. Solutions of Hamiltonian by the method of two outgoing waves

We will now solve the Schrödinger equation,

$$\hat{\mathcal{H}}|\psi\rangle = E|\psi\rangle, \tag{12}$$

for the resonant states $|\psi\rangle$ of the Hamiltonian given in Eq. (4). As has been previously shown,[27,28] the resonant eigenfunction of the tight-binding model on a chain with an adatom can be written in the form

$$\psi_\sigma(x) \equiv \langle x,\sigma|\psi\rangle = A_\sigma e^{iK_\sigma|x|} \tag{13}$$

or

$$\vec{\psi}_\sigma(x) \equiv \begin{pmatrix}\psi_+(x)\\ \psi_-(x)\end{pmatrix} = A_+ e^{iK_+|x|}\begin{pmatrix}1\\0\end{pmatrix} + A_- e^{iK_-|x|}\begin{pmatrix}0\\1\end{pmatrix}. \tag{14}$$

Using the resonant eigenfunction [Eq. (13)] in the Schrödinger equation [Eq. (12)] for the case $x \neq 0$, we obtain

$$\begin{aligned}E\psi_\sigma(x) &= \hat{\mathcal{H}}\psi_\sigma(x) \\ &= -\frac{t_h}{2}\{\psi_\sigma(x+1) + \psi_\sigma(x-1)\} - \sigma t_h'\psi_\sigma(x) \\ &= (-t_h\cos K_\sigma - \sigma t_h')\psi_\sigma(x).\end{aligned} \tag{15}$$

This again yields the dispersion relations $E = -t_h\cos K_\pm \mp t_h'$ inside the two channels of the wire as given in Eq. (7) above.

To solve the eigenequation

$$\psi_d \equiv \langle d|\psi\rangle \quad \text{and} \quad \psi(x,y) \equiv \langle x,y|\psi\rangle \tag{16}$$

for $x=0$ and ψ_d, respectively, we return to the original y space. Using the original bases $|x,y\rangle$ and Eq. (2), the resonant eigenfunctions $\psi(x,y)$

$$\begin{aligned}\vec{\psi}_y(x) &\equiv \begin{pmatrix}\psi(x,1)\\ \psi(x,2)\end{pmatrix} \\ &= U\vec{\psi}_\sigma(x) \\ &= \frac{1}{\sqrt{2}}A_+ e^{iK_+|x|}\begin{pmatrix}1\\1\end{pmatrix} + \frac{1}{\sqrt{2}}A_- e^{iK_-|x|}\begin{pmatrix}1\\-1\end{pmatrix}.\end{aligned} \tag{17}$$

With Hamiltonian (1) the Schrödinger equations [Eq. (12)] for $x=0$ and ψ_d become

$$-\frac{t_h}{2}\{\psi(-1,1) + \psi(1,1)\} - t_h'\psi(0,2) + g\psi_d = E\psi(0,1),$$

$$-\frac{t_h}{2}\{\psi(-1,2) + \psi(1,2)\} - t_h'\psi(0,1) = E\psi(0,2),$$

$$g\psi(0,1) + E_d\psi_d = E\psi_d.$$

Substituting the resonant wave functions ψ in the site representation from Eq. (17) while making use of the continuous dispersion relations [Eq. (7)], we obtain

$$it_h A_+ \sin K_+ + it_h A_- \sin K_- - \sqrt{2}g\psi_d = 0,$$

$$it_h A_+ \sin K_+ - it_h A_- \sin K_- = 0,$$

$$g(A_+ + A_-) + \sqrt{2}(E_d - E)\psi_d = 0, \tag{18}$$

which can be written in matrix form as

$$\begin{pmatrix} it_h \sin K_+ & it_h \sin K_- & -\sqrt{2}g \\ it_h \sin K_+ & -it_h \sin K_- & 0 \\ g & g & \sqrt{2}(E_d - E) \end{pmatrix} \begin{pmatrix} A_+ \\ A_- \\ \psi_d \end{pmatrix} = 0. \tag{19}$$

In order to have nontrivial solutions to Eq. (19), the determinant of the coefficient matrix above must be zero. Hence we obtain the following condition on A_+, A_-, and ψ_d:

$$E - E_d = g^2 \left(\frac{1}{2it_h \sin K_+} + \frac{1}{2it_h \sin K_-} \right). \tag{20}$$

Making use of the channel dispersion equations [Eq. (7)], we can see that the above condition is equivalent to the dispersion equation for embedded electron (11) related to the interaction between the adatom and the two σ channels.

According to the previous work,[2,27] the dispersion equation for the single-chain model with an adatom is given by

$$E_{chain} - E_d = \frac{g^2}{2it_h \sin K_{chain}}. \tag{21}$$

Hence we note that the dispersion equation [Eq. (20)] for the ladder model corresponds to the sum of two single-chain dispersion equations.

In the case of the single-chain model,[2,6,27] the complex energy spectrum could be evaluated in terms of a complex plane consisting of two Riemann sheets. In that case there was only one wave number K_{chain} corresponding to the single channel available to an electron. One can then easily classify whether a resonant state lies in the first or second Riemann sheet according to the sign of the imaginary component of this wave number. For instance, the position of the poles may also influence the strength of the non-Markovian decay due to the so-called branch-point effect (this will be the subject of a future publication).

In the present case of the two-channel model, there are two wave numbers $K_\pm$ resulting from the two channels available to the electron. The imaginary part of these two wave numbers together provides four possible sign combinations and hence the complex energy plane is now composed of four Riemann sheets (see Fig. 3 for an example in the case $0 < t_h' < t_h$). We can also see that the Riemann surface must be four sheeted by considering the dispersion equation [Eq. (11)], in which each of the two roots may take either a positive or negative sign, again resulting in four combinations (although one must be careful here as the sign combinations in this approach change for different portions of the same sheet). In the general case of an n-channel quantum wire, the complex energy surface will be composed of $2n$ Riemann sheets.

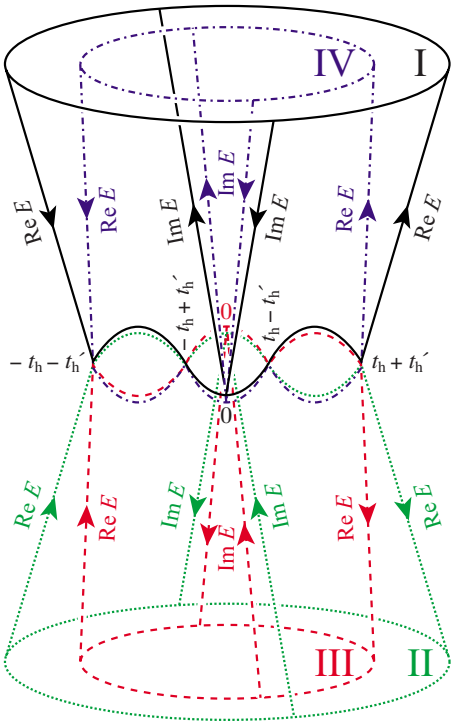

FIG. 3. (Color online) Four-sheeted Riemann energy surface for the two-channel model in the case $0 < t_h' < t_h$. Solutions of the discrete dispersion equation with the sign combination $[\mathrm{sgn}(\mathrm{Im}\, K_+), \mathrm{sgn}(\mathrm{Im}\, K_-)] = (+,+)$ lie in the first Riemann sheet (solid black line). Solutions with the combination $(-,+)$ lie in sheet II (short-dashed green line), those with the combination $(+,-)$ line in sheet III (long-dashed red line), and those with the combination $(-,-)$ lie in sheet IV (chained blue line). The curved lines in the center of the diagram represent the two branch cuts where the sheets intersect along their respective real axes. For instance, on the left side of the diagram, if one starts from the positive imaginary half of sheet I and crosses the real axis between $-t_h - t_h'$ and $-t_h + t_h'$ (represented by the curved overlapping solid black and short-dashed green lines) then one will emerge on the negative imaginary half of sheet II.

For the purpose of assignment of each solution to the correct Riemann sheet, it is more convenient to modify Eq. (20) with the help of the dispersion equations for the continua [Eq. (7)] and solve the following set of simultaneous equations with respect to $K_\pm$ than to solve the dispersion equation for the adatom [Eq. (11)] with respect to $z = E$,

$$-t_h \cos K_+ - t_h' = -t_h \cos K_- + t_h' = E_d + g^2 \left(\frac{1}{2it_h \sin K_+} + \frac{1}{2it_h \sin K_-} \right). \tag{22}$$

The signs of $\mathrm{Im}\, K_\pm$ of each solution give the correct Riemann sheet immediately.

Note that the first Riemann sheet is assigned in a natural way as the energy eigenvalues of all of the solutions in this

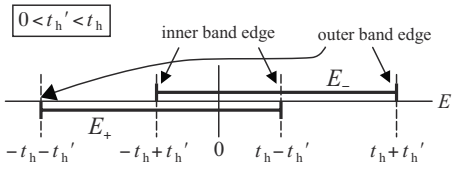

FIG. 4. Band structure for the case $0<t_h'<t_h$. See Eq. (7) for the definition of $E_\pm$.

sheet must be real, each corresponding to a bound state in the energy spectrum analysis (in the complex $K_\pm$ sheets, these solutions lie on the positive imaginary axis). This is because the Hamiltonian must behave in a manner equivalent to a Hermitian operator in this first sheet with all eigenvalues being purely real. It is only when the Hamiltonian is extended into the rigged Hilbert space[31] that complex solutions in the other sheets may be considered on a more equal footing with the stable solutions in the first sheet and that they can be interpreted as complex eigenvalues of the Hamiltonian in the rigged Hilbert space.[32,33]

III. ENERGY SPECTRUM ANALYSIS FOR $0<t_h'<t_h$ AND QBIC STATES

In this section we analyze the eigenenergy spectrum for the case $0<t_h'<t_h$, in which the two conduction bands overlap as in Fig. 2. In this overlapping case the edge of one band is embedded in the continuum of the other and vice versa. This results in two outer band edges and two inner (embedded) band edges (see Fig. 4).

When the energy of the impurity E_d lies inside the overlapping region between the two inner band edges $(-t_h+t_h' < E_d < t_h-t_h')$, we will find that there exist persistent stable solutions that lie just outside of the two outer band edges, as mentioned in Sec. I.[2,4–6] As we will see, these stable states are a direct result of the van Hove singularity in the density of states at the band edge. For the inner band edges, however, there will now be two competing effects: the first being the stabilizing effect of the singularity from the embedded band edge and the second being the destabilizing effect of the continuum in which it is embedded (i.e., the second conduction band). This will result in a slightly destabilized state embedded in the continuum (the QBIC state).

A. Energy spectrum analysis from the dispersion polynomial

We will now analyze in detail the 12 solutions to the dispersion equation for the discrete adatom site [Eq. (11)]. Before presenting the full complex energy spectrum as a function of E_d, we will first consider the eigenenergies at two specific values of E_d in Tables I and II in order to illustrate our earlier point regarding the placement of the solutions in the complex energy surface. In these tables, we present the values obtained for each of the 12 solutions by solving the dispersion equation [Eq. (11)] for the eigenenergies E and the channel dispersion equations [Eq. (7)] for the wave number pairs $K_\pm$ at the two values $E_d=0.3$ and $E_d=-1.0$, respectively. For the other parameters of the system, in both tables we have used the values $t_h'=0.345$ and $g=0.1$. In these tables (and throughout this paper) we measure energy in units $t_h=1$. In addition, in Fig. 5 we have indicated the relative position of each individual pole in the complex K_+, K_-, and E planes, each given for the value $E_d=0.3$ from Table I.

As mentioned previously, the placement of each solution in the complex energy plane can be determined in a straight-

TABLE I. The 12 discrete eigenvalues for $t_h'=0.345$, $g=0.1$, and $E_d=0.3$. (Energy is measured in units of $t_h=1$.) The decay solutions are indicated by underlining.

State	E		K_+		K_-		Riemann sheet
P1(0.3)	1.34501152		3.14159265	$+i$ 1.11593256	3.14159265	$+i$ 0.00480148	I
P2(0.3)	−1.34500463			$+i$ 0.00304629		$+i$ 1.11592751	I
Q1(0.3)	1.34501136		3.14159265	$-i$ 1.11593245	3.14159265	$+i$ 0.00476787	II
Q2(0.3)	−0.65501370	$-i$ 1.5093×10^{-7}	1.25558888	$-i$ 1.5875×10^{-7}	−0.00002882	$+i$ 0.00523534	II
Q3(0.3)	−0.65501370	$+i$ 1.5093×10^{-7}	−1.25558888	$-i$ 1.5875×10^{-7}	0.00002882	$+i$ 0.00523534	II
RQ4(0.3)	0.29998854	$-i$ 0.00153774	2.27180290	$-i$ 0.00201224	−1.52576970	$+i$ 0.00153930	II
RQ5(0.3)	0.29998854	$+i$ 0.00153774	−2.27180290	$-i$ 0.00201224	1.52576970	$+i$ 0.00153930	II
R1(0.3)	−1.34500459			$+i$ 0.00303273		$-i$ 1.11592748	III
R2(0.3)	0.65509906	$-i$ 2.9331×10^{-6}	−3.14138429	$+i$ 0.01407702	1.88609355	$-i$ 3.0852×10^{-6}	III
R3(0.3)	0.65509906	$+i$ 2.9331×10^{-6}	3.14138429	$+i$ 0.01407702	−1.88609355	$-i$ 3.0852×10^{-6}	III
S1(0.3)	0.29991927	$-i$ 0.01154476	2.27161773	$-i$ 0.01510419	1.52570333	$-i$ 0.01155625	IV
S2(0.3)	0.29991927	$+i$ 0.01154476	−2.27161773	$-i$ 0.01510419	−1.52570333	$-i$ 0.01155625	IV

TABLE II. The 12 discrete eigenvalues for $t_h'=0.345$, $g=0.1$, and $E_d=-1.0$. (Energy is measured in units of $t_h=1$.) The decay solutions are indicated by underlining.

State	E		K_+		K_-		Riemann sheet
P1(−1)	1.34500228		3.14159265	$+i$ 1.11592578	3.14159265	$+i$ 0.00213553	I
P2(−1)	−1.34510721			$+i$ 0.01464344		$+i$ 1.11600280	I
Q1(−1)	1.34500226		3.14159265	$-i$ 1.11592577	3.14159265	$+i$ 0.00212886	II
Q2(−1)	−1.00545676	$-i$ 0.00659855	0.84940336	$-i$ 0.00878757	−0.00726999	$+i$ 0.81454288	II
Q3(−1)	−1.00545676	$+i$ 0.00659855	−0.84940336	$-i$ 0.00878757	0.00726999	$+i$ 0.81454288	II
R1(−1)	−1.34510275			$+i$ 0.01433550		$-i$ 1.11599952	III
R2(−1)	0.65500456	$-i$ 2.9002×10^{-8}	−3.14158305	$+i$ 0.00302110	1.88599415	$-i$ 3.0505×10^{-8}	III
R3(−1)	0.65500456	$+i$ 2.9002×10^{-8}	3.14158305	$+i$ 0.00302110	−1.88599415	$-i$ 3.0505×10^{-8}	III
RQ4(−1)	−0.65510500	$+i$ 3.2049×10^{-6}	1.25549284	$+i$ 3.3711×10^{-6}	−0.00022112	$-i$ 0.01449328	III
RQ5(−1)	−0.65510500	$-i$ 3.2049×10^{-6}	−1.25549284	$+i$ 3.3711×10^{-6}	0.00022112	$-i$ 0.01449328	III
S1(−1)	−0.99434007	$-i$ 0.00663666	0.86411247	$-i$ 0.00872637	0.00744838	$-i$ 0.80218340	IV
S2(−1)	−0.99434007	$+i$ 0.00663666	−0.86411247	$-i$ 0.00872637	−0.00744838	$-i$ 0.80218340	IV

forward manner by the sign of the imaginary parts of the two complex wave vectors $K_\pm$, which are given as the solutions of the simultaneous equations [Eq. (22)] (see Fig. 6). We have designated those with positive imaginary K_+ component and positive imaginary K_- component [(+,+), respectively] as lying in Riemann sheet I; likewise we have designated (−,+) as sheet II, (+,−) as sheet III, and (−,−) as sheet IV. The resulting eigenenergy $E=-t_h\cos K_\pm \mp t_h'$ of each solution is shown in Fig. 7. In Tables I and II and Figs. 6 and 7, we have labeled each solution by a letter P, Q, R, or S according to the Riemann sheet (I, II, III, or IV, respectively) in which that solution lies.

As these solutions are roots of a polynomial with real coefficients, each complex decay solution (with negative imaginary part) is accompanied by a complex conjugate "growth" solution with positive imaginary part. However, when we calculate the survival probability for the excited impurity state, only the decay solutions will contribute a pole in the complex contour integration. Hence, our focus will be the decay solutions indicated by shading in Tables I and II.

Note that sheet I contains only purely real solutions. This choice is necessary so that our system with complex eigenvalues (higher sheets) in the rigged Hilbert space simplifies to that of real eigenvalues in the ordinary Hilbert space in the finite case (closed system) or when the coupling vanishes. Also notice that there is one conjugate pair of solutions (RQ4 and RQ5) labeled by two sheets. This is due to the fact that these solutions lie in sheet III for negative values of E_d and then cross into sheet II (through the double branch cut on the real axis of the complex energy plane) for positive values of E_d. At the same time, the imaginary part of the energy eigenvalue changes its sign; solution RQ5 is the decay solution for $E_d<0$, but RQ4 gives the decay solution for $E_d>0$. These two solutions disappear for the case $t_h=t_h'$ as will be discussed in Sec. V.

We now analyze the detailed energy spectrum for our ladder model in the present $0<t_h'<t_h$ case. In Fig. 8 we present the real part of the 12 solutions of the dispersion equation

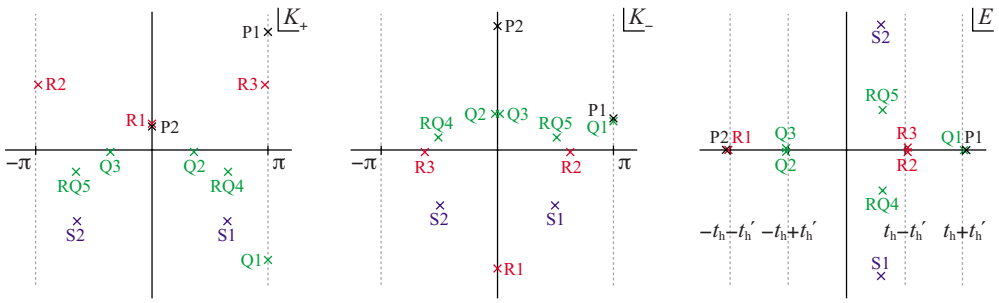

FIG. 5. (Color online) The relative positions of the poles in the complex K_+, K_-, and E planes for the value $E_d=0.3$, as well as $t_h'=0.345$ and $g=0.1$, as given in Table I. The two vertical dotted lines in (a) and (b) indicate the edges of the Brillouin zone Re $K_\pm=\pm\pi$, while the four vertical dotted lines in (c) represent the van Hove singularities (at the four band edges).

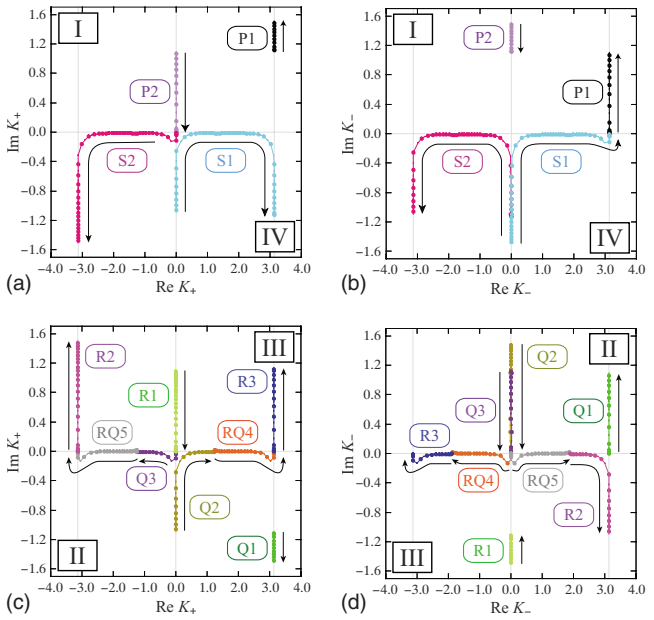

FIG. 6. (Color online) The wave numbers $K_\pm$ for the 12 solutions of the set of Eq. (22). The arrows represent how the solutions move when we increase E_d from −2 to 2 with $t_h'=0.345$ and $g=0.1$, where energy is measured in units of $t_h=1$. The left-hand (a) and (c) show the K_+ plane and the right-hand (b) and (d) show the K_- plane. In the top, (a) and (b), the solutions in the upper half plane are in Riemann sheet I and those in the lower half plane are in Riemann sheet IV. In (c), the solutions in the lower half plane are in Riemann sheet II and those in the upper half plane are in Riemann sheet III. In (d), the solutions in the upper half plane are in Riemann sheet II and those in the lower half plane are in Riemann sheet III. In the bottom (c) and (d), solutions RQ4 and RQ5 cross the real axes from Riemann sheet III into Riemann sheet II when E_d is increased from negative to positive. The vertical gray lines represent $K_\pm=-\pi,0,\pi$.

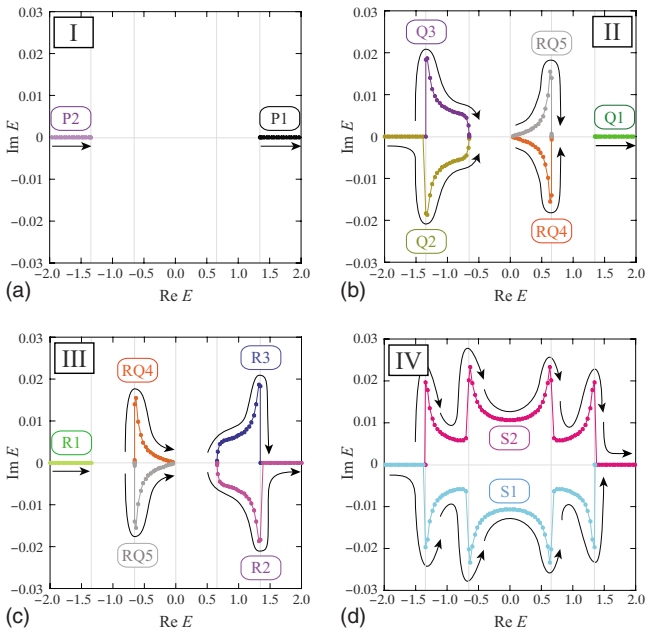

FIG. 7. (Color online) The complex energy (parametrized as a function of E_d) for the 12 solutions of the dispersion equation, with each energy placed in the appropriate Riemann sheet(s). The arrows represent how the solutions move when we increase E_d from −2 to 2 with $t_h'=0.345$ and $g=0.1$. Energy is measured in units of $t_h=1$. The vertical gray lines represent the four van Hove singularities.

[Eq. (11)] as a function of the impurity energy E_d. We have also plotted the line Re $E=E_d$ that represents the unperturbed energy of the adatom for $g=0$. Hence, the deviation of each solution from this line represents the energy shift due to the interaction with the two-channel wire. Then in Fig. 9 we present the imaginary part of the eight complex solutions.

The behaviors of the two purely real solutions P2 and R1 [Fig. 8(e)] are consistent with the energy spectrum previously pointed out[2,5,6] for the persistent stable states mentioned above. For values of $E_d \ll -t_h-t_h'$ far below the lowest band edge, these two solutions are shifted downward slightly from the line Re $E=E_d$. (The shift for both solutions can be shown to be proportional to g^2, though P2 always has the slightly larger shift.) For values $E_d \gg -t_h-t_h'$ anywhere above the lowest band edge we find these solutions are shifted downward instead from the lowermost band edge Re $E=-t_h-t_h'$, consistent with the previously reported behavior for the persistent stable state. In Sec. III B 1, we will show that in this case the shift is proportional to g^4.

For values $E_d \ll -t_h-t_h'$ we find that solutions S1 and S2 [lower left-hand corner of Fig. 8(d)] are also purely real. Since these real states do not lie in the first Riemann sheet, they are antibound states or virtual states.[34,35] As we increase the value of E_d such that $E_d \lesssim -t_h-t_h'$ we find that these solutions merge abruptly to form a complex conjugate pair [Fig. 8(d)]. This is similar to the behavior of the complex solutions in the single-channel model.[2] The imaginary part of these solutions can be seen in Fig. 9(d) and in detail in Fig. 10. Notice in these figures that the decay rate is amplified for S1 and S2 in the vicinity of each of the four band edges. This amplification is a result of the breakdown of Fermi's golden rule in the vicinity of the van Hove singularity at each of the band edges. Ordinarily, the golden rule predicts that to lowest order the decay rate will be proportional to the square of the coupling constant g^2. In our case, we can see Fermi's golden rule in Eq. (11). If a solution $z=E$ of the dispersion equation [Eq. (11)] is far away from any band edges $\pm t_h \pm t_h'$, it would behave as $E \simeq E_d + O(g^2)$ or $|\text{Im } E| \sim O(g^2)$. However, the van Hove singularity in the context of a one-dimensional system results in a decay rate with a nonanalytic dependence on the coupling constant, such that to lowest order the decay rate is proportional to $g^{4/3}$, as previously reported.[2,5] In Sec. IV A we will take a closer look at this effect and study the behavior of the system in the crossover between the region where Fermi's rule is valid and the amplification region near the singularity where the golden rule breaks down. For now we focus on the QBIC effects.

B. van Hove singularity and the origin of the quasibound states in continuum

We will now consider the detailed behavior and the origin of the QBIC effect. The decaying solutions Q2, R2, and RQ4 (or RQ5) [and their conjugate growth partners Q3, R3, and

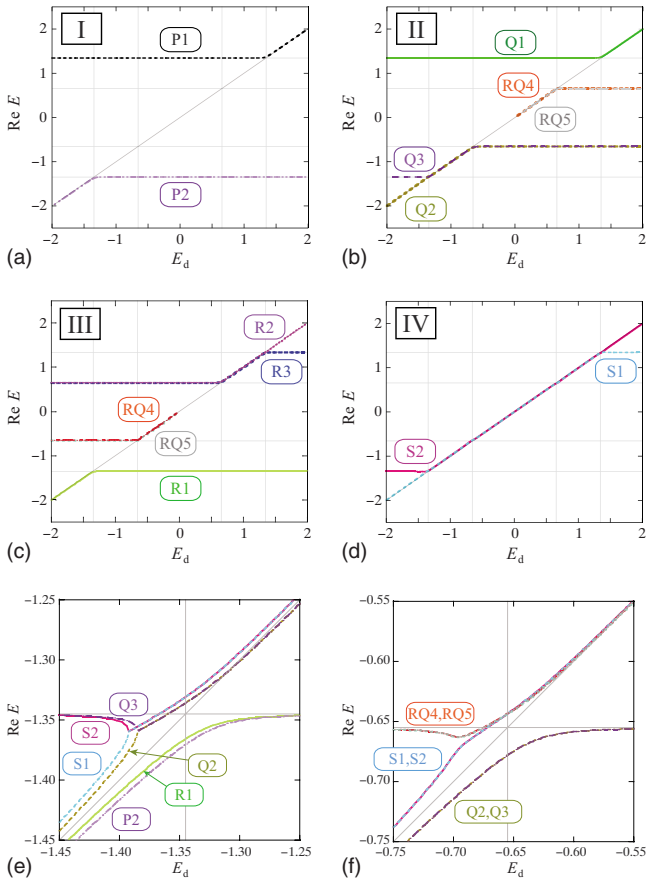

FIG. 8. (Color online) Real part of the energy for the 12 solutions of the dispersion equation as a function of E_d for the values $t_h'=0.345$ and $g=0.1$. Energy is measured in units of $t_h=1$. In the top, (a)–(d), each solution is plotted in the corresponding Riemann sheet. The overlapping curves represent a complex conjugate pair, for which the real part of the energy is exactly the same. The vertical and horizontal gray lines represent the four van Hove singularities. In the bottom, (e) and (f), portions of the top (a)–(d) are shown with all four Riemann sheets superimposed.

RQ5 (or RQ4), respectively] each displays this effect in different regions of the energy spectrum. Here we will focus on solution Q2 as our example in order to demonstrate the properties of the QBIC states. Taking symmetry into account (see Fig. 9), solution R2 behaves in a manner almost analogous to Q2. Meanwhile a detailed analysis of the integration contour for the survival probability of the excited state reveals that solutions RQ4 and RQ5 may be of less significance in terms of the QBIC effect as they do not contribute a pole (exponential decay) in this calculation. These solutions may play a more significant role in terms of the non-Markovian decay. However, we do not discuss this subject in the present paper.

Focusing on solution Q2, we see in Figs. 8 and 9(b) that the solution is complex with substantial imaginary part for values of the impurity energy E_d below the lower inner band edge $-t_h+t_h'$. Specifically in the range $-t_h-t_h' \ll E_d \ll -t_h+t_h'$ (between the lower outer band edge and the lower inner band edge), solution Q2 is close to E_d with decay rate consistent with Fermi's golden rule. In this region, let us expand solution Q2 around E_d as

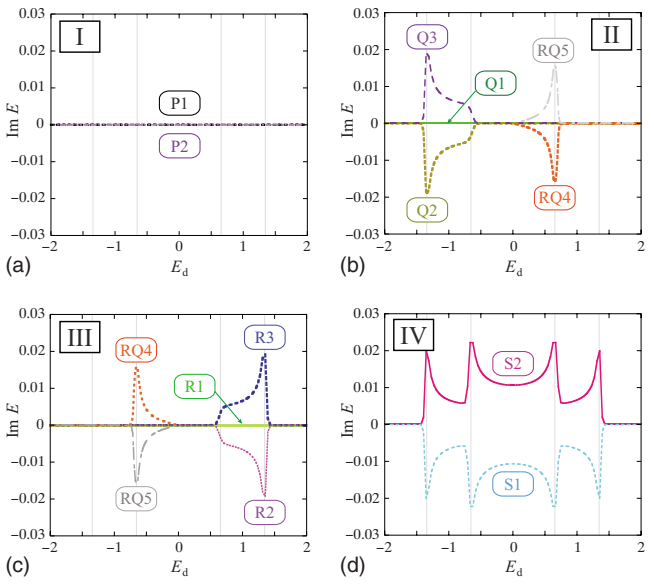

FIG. 9. (Color online) Imaginary part of the energy for the eight complex solutions of the dispersion equation as a function of E_d for the values $t_h'=0.345$ and $g=0.1$. The unit of the energy is $t_h=1$. The vertical gray lines represent the four van Hove singularities.

$$E_{Q2} = E_d + \chi_2 g^2 + \chi_4 g^4 + \ldots . \tag{23}$$

Using this expansion ansatz in the dispersion equation [Eq. (11)], we find that the expansion is indeed consistent and we have

$$\chi_2 = \frac{1}{2}\left[-\frac{i}{\sqrt{(E_d+t_h')^2 - t_h^2}} - \frac{1}{\sqrt{t_h^2 - (E_d - t_h')^2}} \right]. \tag{24}$$

These terms give the first-order decay rate and energy shift, respectively. We see that the decay rate is given by $|\mathrm{Im}\, E_{Q2}| \sim O(g^2)$ and is proportional to the density of states $\rho_+(E)$ in the lower channel. Both of these behaviors are consistent with Fermi's golden rule.

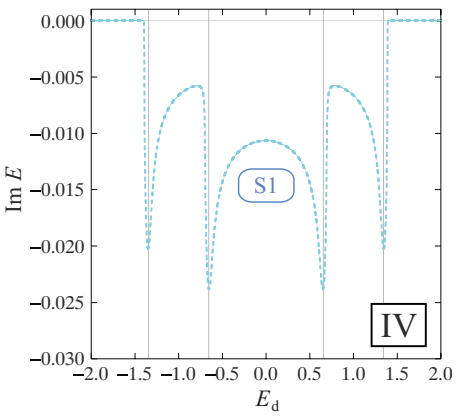

FIG. 10. (Color online) Imaginary part of the energy (decay rate) for solution S1 (sheet IV) as a function of E_d for the values $t_h'=0.345$ and $g=0.1$. The unit of the energy is $t_h=1$. The vertical gray lines represent the four van Hove singularities, just as in Fig. 9. The decay rate for S1 is amplified (such that $\mathrm{Im}\, E \sim g^{4/3}$) in the vicinity of each of the band edges due to the singularities.

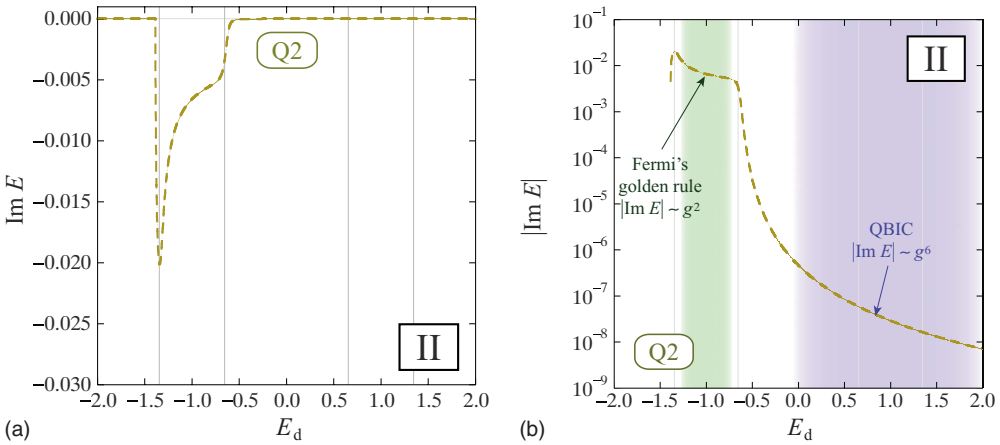

FIG. 11. (Color online) (a) A linear plot and (b) a semilogarithmic plot of the imaginary part of the energy (decay rate) for solution Q2 (sheet II) as a function of E_d for the values $t_h'=0.345$ and $g=0.1$. The unit of the energy is $t_h=1$. The vertical gray lines represent the four van Hove singularities, just as in Fig. 9. For solution Q2, the decay rate is amplified (such that Im $E\sim g^{4/3}$) in the vicinity of the lowest outer band edge $-t_h-t_h'$. For the portion of the spectrum between $-t_h-t_h'$ and the lower inner band edge $-t_h+t_h'$, Q2 has an ordinary decay rate Im $E\sim g^2$. This portion is indicated by green shading in (b). For values of $E_d \gg -t_h+t_h'$ the decay rate becomes exceedingly small (with Im $E\sim g^6$) as the solution behaves as a full QBIC state. This region is shaded blue in the semilogarithmic plot (b) above. We will study the portion of the spectrum between these two regions later on in Secs. III C 5 and III C 6.

However, in Figs. 8(b) and 8(f) we see that as we increase the value of E_d, the real part of E_{Q2} departs from E_d and approaches the inner band edge $-t_h+t_h'$ in a manner similar to the persistent bound state P2 discussed above. Meanwhile, the imaginary component of E_{Q2} does not vanish near the inner band edge. Instead, the decay rate lies near the value zero as can be seen in Fig. 9(b) and in greater detail in Fig. 11. This is the QBIC state introduced in our previous letter.[1] As can be seen from the figures, the real part of the energy is embedded in the lower energy band similar to the bound states in continuum proposed by von Neumann and Wigner, while the decay rate is nonzero but remarkably small. This behavior for state Q2 occurs over a wide range of the energy spectrum, specifically for all values of the impurity energy that are far above the value of this inner band edge $E_d \gg -t_h+t_h'$. We label this region in the semilogarithmic plot in Fig. 11(b).

We will now show that the QBIC effect is a direct result of two competing effects resulting from the embedding of the van Hove singularity at the edge of one conduction band in the continuum of the other band. The first effect is the tendency of the embedded singularity to create a persistent bound state; in other words, there would be an ordinary persistent stable state if it was not for the second energy band. The second effect is the tendency of the embedding conduction band to destabilize an otherwise stable state. In order to make this point explicit, we will obtain an analytic expansion for the energy eigenvalue of the persistent stable state in a single-channel model (see Fig. 12) and compare this term by term with a similar expansion for QBIC state Q2 in the present case (see Fig. 13). This follows from our discussion in the previous letter.[1]

1. Analytic approximation for the eigenenergy for the persistent stable state in the single-channel model

We may write the Hamiltonian $\hat{\mathcal{H}}_-$ for a single-channel quantum wire[36] with energy shifted by t_h' as

$$\hat{\mathcal{H}}_- = -\frac{t_h}{2}\sum_x (|x+1\rangle\langle x| + |x\rangle\langle x+1|) + t_h' + \frac{g}{\sqrt{2}}(|d\rangle\langle 0,1| + |0,1\rangle\langle d|) + E_d|d\rangle\langle d|. \quad (25)$$

We have chosen the energy offset t_h' here such that the single energy band for this Hamiltonian mimics that of the upper energy band ($E_-=-t_h \cos K_- + t_h'$) in the two-channel model. This single channel will also have the same density of states function ρ_- from Eq. (8). Then the exact form of the dispersion equation for the adatom in the single-channel case[2,4,6,27] is given by

$$z - E_d - \frac{g^2}{2}\left[\frac{1}{\sqrt{(z-t_h')^2 - t_h^2}}\right] = 0. \quad (26)$$

This is equivalent to a quartic dispersion polynomial after squaring. Note the presence of the singularities in the third term at $z=\pm t_h+t_h'$; these are a result of the singularities in the density of states function ρ_- just as in the two-channel case.

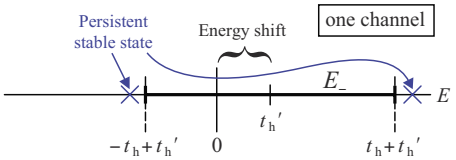

FIG. 12. (Color online) Diagrammatic representation of the upper energy band E_- associated with the (shifted) single-channel Hamiltonian $\hat{\mathcal{H}}_-$ and the purely real energy associated with the persistent stable state E_{ps} (our focus in the text is on the lower solution near $-t_h+t_h'$).

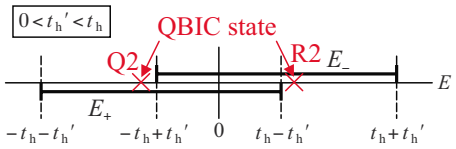

FIG. 13. (Color online) Diagrammatic representation of the two energy bands $E_{\pm}$ associated with the full two-channel Hamiltonian $\hat{\mathcal{H}}$ of Eq. (1) and the real part of the energy associated with the quasibound state in continuum E_{Q2} (E_{R2}) that lies below the lower inner band edge at $-t_h+t_h'$ (above the upper inner band edge at t_h-t_h'). Our focus in the text is on the solution E_{Q2}.

Now we will obtain an approximate form for the energy of the persistent stable state as a solution E_{ps} of the single-channel discrete dispersion equation [Eq. (26)]. This approximation will hold under the assumption that the impurity energy is much larger than that of the lower inner energy band, that is, $E_d \gg -t_h+t_h'$. The energy of this persistent stable state and its relation to the energy band E_- are represented diagrammatically in Fig. 12; the definition of E_- is given in Eq. (7). Considering this observation, we write an expansion for E_{ps} near the lower band edge $-t_h+t_h'$ in powers of the coupling constant as

$$E_{ps} = (-t_h + t_h') + \chi_\alpha g^\alpha + \chi_\gamma g^\gamma + \ldots, \tag{27}$$

in which $0<\alpha<\gamma$ and $|\chi_i| \sim 1$ is independent of the coupling g at every order. The power of g in each term is to be determined below. Notice that we have "skipped" the β term in Eq. (27); this is in anticipation of the appearance of the decay rate in a similar approximation that we will perform for the QBIC state further on [cf. Eq. (35)].

We can now use Eq. (27) to write the dispersion equation [Eq. (26)] as

$$E_{ps} - E_d = \frac{g^2}{2} \frac{1}{\sqrt{-2t_h\chi_\alpha g^\alpha - 2t_h\chi_\gamma g^\gamma + O(g^{\alpha+\gamma}, g^{2\alpha})}}. \tag{28}$$

We can expand this to obtain

$$(-t_h + t_h' - E_d) + \chi_\alpha g^\alpha + \chi_\gamma g^\gamma \approx \frac{g^{2-\alpha/2}}{2\sqrt{-2t_h\chi_\alpha}} + g^{2-\alpha/2} O(g^{\gamma-\alpha}, g^\alpha). \tag{29}$$

The term in parentheses on the left-hand side (LHS) and the first term on the right-hand side (RHS) represent the two lowest-order terms. We therefore equate them,

$$(-t_h + t_h' - E_d) = \frac{g^{2-\alpha/2}}{2\sqrt{-2t_h\chi_\alpha}}. \tag{30}$$

This can be shown to be the only consistent choice. Since the term in parentheses is zeroth order in g, equating these terms gives the condition $2-\alpha/2=0$ or $\alpha=4$, as well as

$$\chi_\alpha = -\frac{1}{8t_h(t_h' - t_h - E_d)^2}. \tag{31}$$

The second-lowest-order correction is then given by equating the second term on the LHS of Eq. (29) with the second term on the RHS,

$$\chi_\alpha g^\alpha = g^{2-\alpha/2} O(g^{\gamma-\alpha}, g^\alpha). \tag{32}$$

This gives $\gamma=2\alpha=8$. Making use of Eq. (31), we can then write the expansion for the real energy for the persistent bound state [Eq. (27)] as

$$E_{ps} = (-t_h + t_h') - \frac{1}{8t_h(t_h' - t_h - E_d)^2} g^4 + O(g^8). \tag{33}$$

We see that the energy shift from the band edge $-t_h+t_h'$ is of order g^4. Notice that it was the cancellation of the band-edge term $-t_h+t_h'$ when we plugged expansion (27) into the square root of Eq. (26) that resulted in the $g^{2-\alpha/2}$ term in Eq. (29); hence the persistent stable state is a direct result of the divergent van Hove singularity at the band edge. Also note that E_{ps} is purely real, including higher orders.

Before returning to the main subject of this Sec. III B, we briefly mention the general conditions for the presence of the persistent stable state for a system with a discrete state (here, the impurity) coupled to a continuum of states through the potential $\nu(E)$. Let us assume the continuum has density of states $\rho(E)$ with divergent singularity at a band edge W. The requirement for the persistent stable state to appear just outside this band edge is simply that the self-energy for the discrete state must diverge at W, which requires[19] that

$$\lim_{E\to W} |\nu(E)|^2 \rho(E) \to \infty, \tag{34}$$

where the divergence must be real. This clearly holds for the single-channel wire at $W=-t_h+t_h'$ with $\nu(E)=g/\sqrt{2}$ and $\rho(E)=\rho_-(E)$. Further then, the energy of the discrete state should be well within the continuum for the persistent bound state to be actually realized. We note that there do exist certain one-dimensional models with the square root form of the DOS singularity in Eq. (8) where nonetheless this condition is not met. This is because the form of the interaction potential may cancel the divergence (the antisymmetric solutions in Ref. 20 and the semi-infinite chain in Ref. 19 give two examples). Condition (34) is also a necessary condition for the QBIC. However, we must make the further condition that the band edge W is embedded in a second continuum, as we discuss in the following calculation.

2. Analytic approximation for QBIC state Q2 in the two-channel model

Now we return to the main subject of this Sec. III B. We will obtain a similar expansion for the energy of QBIC state Q2 in the case of the two-channel model. We again present a diagrammatic representation of the energy of this state and its relation to the two energy bands in Fig. 13. As before, if we assume that $E_d \gg -t_h+t_h'$, then the real part of the energy of Q2 will be shifted such that it lies slightly below the lower edge of the upper energy band at $-t_h+t_h'$ just as in the case of

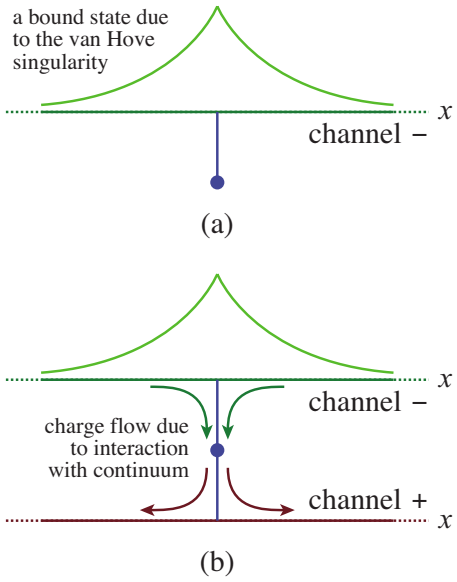

FIG. 14. (Color online) (a) A schematic view of the persistent bound state (due to the van Hove singularity) of a one-channel system with the eigenvalue just below the lower band edge. (b) Some of the bound particles leak into the attached channel in the two-channel model, which destabilizes the bound state.

the persistent stable state. However, in this case the band edge (and therefore the energy of state Q2 as well) is embedded in the continuum of the lower energy band. It is well known that the continuum will usually have a destabilizing effect on a discrete state that is embedded within it. In this case the embedding will result in a slight destabilization of the otherwise stable state. For a further illustration of the relationship between the persistent stable state and the QBIC state, refer to Figs. 14(a) and 14(b).

As before, we write the expansion for the energy of state Q2 as

$$E_{Q2} = (-t_h + t_h') + \chi_\alpha g^\alpha + \chi_\beta g^\beta + \chi_\gamma g^\gamma + \ldots, \tag{35}$$

where $0<\alpha<\beta<\gamma$. Here we have included the β term; below we will see that this term results in the small decay rate giving the QBIC effect. The zeroth-order term $-t_h+t_h'$ places the solution well inside the continuum of the lower energy band E_+. Looking to discrete dispersion relation (11), we note that it is the second term in the square brackets that is associated with the upper energy band E_- including the embedded band edge at $-t_h+t_h'$; the first term is associated with the embedding lower energy band E_+.[37]

Putting expansion (35) into Eq. (11), we obtain

$$\begin{aligned}(-t_h + t_h' - E_d) + \chi_\alpha g^\alpha + \chi_\beta g^\beta + \chi_\gamma g^\gamma &\approx \left(\frac{g^{2-\alpha/2}}{2\sqrt{-2t_h\chi_\alpha}} - \frac{\chi_\beta g^{\beta-\alpha+(2-\alpha/2)}}{4\sqrt{-2t_h\chi_\alpha^3}} + g^{2-\alpha/2} O(g^{\gamma-\alpha}, g^\alpha, g^{2(\beta-\alpha)}) \right) \\ &+ \left(\frac{g^2}{2\sqrt{(2t_h'-t_h)^2 - t_h^2}} + O(g^{\alpha+2}) \right).\end{aligned} \tag{36}$$

We note that in expression (36) the terms in the first set of parentheses on the RHS are associated with the embedded singularity at $-t_h+t_h'$ and those in the second set of parentheses are associated with the embedding continuum. We will see that equating one term from each results directly in the QBIC effect. The essential difference from expansion (29) for the single-channel model is the existence of the terms in the second set of parentheses on the RHS. These terms came from the first term in the square brackets of Eq. (11), which is missing in the dispersion equation [Eq. (26)] for the single-channel model. These terms give rise to the β term in Eq. (35).

The lowest-order correction is obtained exactly as in the case of the persistent stable state above; by equating the first term on the LHS with the first term in the first set of parentheses on the RHS as

$$(-t_h + t_h' - E_d) = \frac{g^{2-\alpha/2}}{2\sqrt{-2t_h\chi_\alpha}}, \tag{37}$$

we obtain the condition $\alpha=4$ and Eq. (31) for χ_α as before. The second-lowest-order condition is then obtained by equating the second term in the first set of parentheses on the RHS of Eq. (36) with the first term in the second set of parentheses on the RHS (associated with the embedded singularity and the embedding continuum, respectively),

$$\frac{\chi_\beta g^{\beta-\alpha+(2-\alpha/2)}}{4\sqrt{-2t_h\chi_\alpha^3}} = \frac{g^2}{2\sqrt{(2t_h'-t_h)^2 - t_h^2}}. \tag{38}$$

This condition did not exist in the previous case of the single-channel model. This gives $\beta-\alpha=2$ or $\beta=6$, as well as

$$\chi_\beta = -\frac{i}{16t_h(t_h'-t_h-E_d)^3\sqrt{t_h'(t_h-t_h')}}. \tag{39}$$

This correction is purely imaginary as $t_h-t_h'>0$ in the case of overlapping bands. This is the QBIC effect, appearing as a second-lowest-order correction. It is a direct result of the interaction of the discrete state with the two overlapping energy bands, as we have just shown. The condition on the remaining terms in Eq. (36),

$$\chi_\alpha g^\alpha \sim g^{2-\alpha/2} O(g^{\gamma-\alpha}, g^\alpha, g^{2(\beta-\alpha)}), \tag{40}$$

yields the consistent result $\gamma=8$ as in the case of the persistent stable state before.

Expansion (35) for state Q2 can now be written as

$$\begin{aligned}E_{Q2} = (-t_h + t_h') &- \frac{1}{8t_h(t_h'-t_h-E_d)^2} g^4 \\ &- i\frac{1}{16t_h(t_h'-t_h-E_d)^3\sqrt{t_h'(t_h-t_h')}} g^6 + O(g^8).\end{aligned} \tag{41}$$

Comparison with Eq. (33) above emphasizes that this state behaves essentially like the persistent stable state that results from the van Hove singularity. The difference is that in this case the energy shift places this state in the continuum of the lower energy band and with a small decay rate at order g^6.

For a numerical comparison, we can plug in the numbers $t_h'=0.345$, $g=0.1$, and $E_d=0.3$ from Table I, where energy is

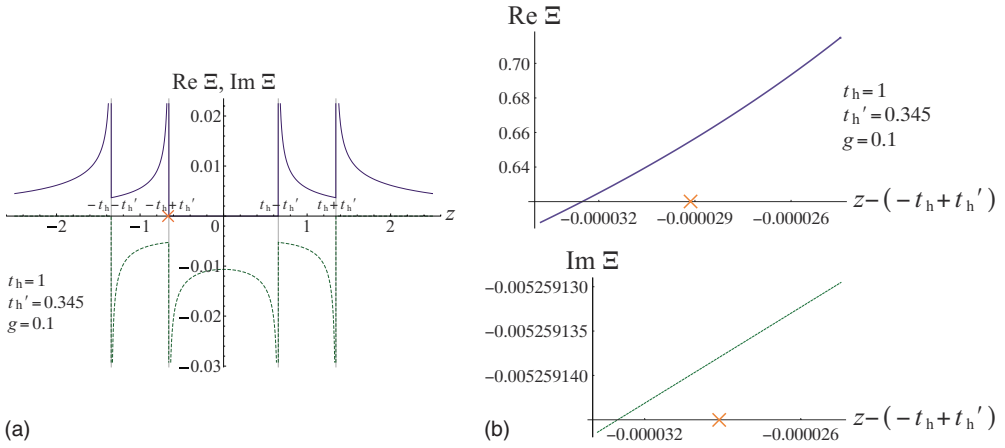

FIG. 15. (Color online) (a) We plot the real part (blue solid line) and the imaginary part (green dashed line) of the self-energy $\Xi(z)$ across the band spectra for the two-channel system, using the usual values $t_h'=0.345$ and $g=0.1$, where energy is measured in units of $t_h=1$. We show the position of the real part of solution Q2 (at $E_d=0$) with an orange X. In (b) we show a magnified view of the real parts (upper half) and the imaginary part (lower half) of $\Xi(z)$ in the vicinity of the lower inner band edge. The z axis of both plots in (b) is measured as a distance from this band edge $-t_h+t_h'$ and is centered on the position of the real part of Q2. The scale of the z axis in the magnified plots is ten times the scale of the imaginary part of Q2 ($\sim g^6$). Note that both curves are fairly smooth despite their proximity to the van Hove singularity in this region.

measured in units of $t_h=1$. Plugging these numbers into Eq. (33) for the persistent stable state in the single-channel case gives $E_{ps}\approx -0.655\,013\,701$ [this value includes the g^8 term not explicitly given in Eq. (33) above]. Plugging the same values into Eq. (41) gives the value $E_{Q2}\approx -0.655\,013\,704 - i(1.5095\times 10^{-7})$ in agreement with the numerically obtained value reported in Table I.

Let us make a few final comments on our expansion. Note that the expression for E_{Q2} given above diverges in the case $t_h'=t_h$. This of course indicates that our expansion breaks down as t_h' approaches t_h. We will find a new expression to replace Eq. (41) in the special case $t_h'=t_h$ in Sec. V. Also, perhaps it is worth noting that in the limit $E_d\to\infty$ the expression for E_{Q2} approaches a purely bound state located exactly at the inner band edge $-t_h+t_h'$. Finally, in the endnotes we mention how to easily transform expression (41) to obtain a similar expansion for state R2, which is also QBIC under the conditions $E_d \ll t_h - t_h'$.[38]

3. Smoothness of self-energy function and general conditions for QBIC state

As a final point regarding the QBIC state in this case, we note that some initial concern might seem warranted in its interpretation as a resonant state with an extremely small lifetime. After all, as we have detailed above, the energy of this state lies in the vicinity of the band edge, exactly where the self-energy contains a divergence. We might expect this to be problematic because the most simple interpretation of the imaginary part of an energy eigenvalue as a decay rate for the corresponding state holds only if the self-energy function $\Xi_d(z)$ given in Eq. (10) varies in a smooth manner in the neighborhood of the energy of this state (the real part of the eigenvalue). The scale of the neighborhood we should consider here is the scale of the decay rate (imaginary part of the eigenvalue).

We check this point in Fig. 15. In Fig. 15(a) we have plotted the real part and the imaginary part of $\Xi_d(z)$ across the width of the band spectra, including the four divergent singularities, using the values $t_h'=0.345$ and $g=0.1$. We have labeled the real part of the pole Q2 (at the representative point $E_d=0$) with an orange "X," which is shifted slightly to the left of the divergence at $z=-t_h+t_h'$. In Fig. 15(b) we have included a split panel with a magnified view of the real part of $\Xi_d(z)$ (upper plot) and the imaginary part (lower plot) centered on the position of the real part of Q2. We have shifted the z axis in these two magnified panels by the value $-t_h+t_h'$ so that this axis is measured as a distance below the inner band edge where Re E_{Q2} lies. Also note that the scale of the z axis in this case varies by one order of magnitude larger than the scale of the decay rate of Q2. As can be seen in Fig. 15(b), both the real part and the imaginary part of $\Xi_d(z)$ are quite smooth over this range of values. Further, in either case they vary over an energy scale that is only a fraction of the characteristic energy of the system $t_h=1$.

Notice in Fig. 15(a) that the real part of the self-energy diverges on the outer side of each of the four band edges. Meanwhile the two regions between the outer band edges $\mp(t_h+t_h')$ and the inner band edges $\mp(t_h-t_h')$ are the only portions of the spectrum in which both the real part and the imaginary part of $\Xi(z)$ are nonzero. This of course is precisely the region where the QBIC states occur. Indeed, recall from Eq. (34) that the condition for the persistent bound state to appear near a band edge is that the real part of the self-energy must diverge at that point. This divergence allows for a very large shift in the perturbed energy (real part of the eigenvalue) away from the original energy E_d, such that the energy eigenvalue "sticks" to the band edge. This occurs for the two-channel model at the outer band edges $\pm(t_h+t_h')$ which gives rise to the persistent bound states P1, P2, Q1, and R1. Meanwhile the QBIC state occurs on the inner band edges precisely because the real part of the self-energy diverges (large energy shift) while the imaginary part remains finite but nonzero (small decay rate). Hence, this behavior of

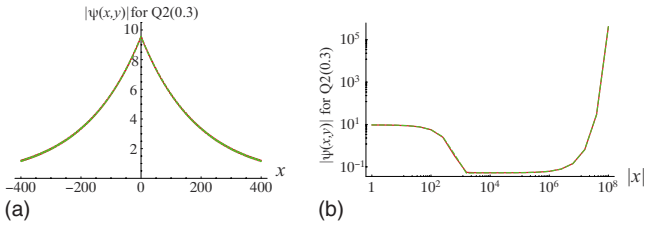

FIG. 16. (Color online) (a) The wave function modulus $|\psi(x,y)|$ of state Q2 around the origin (linear scale) in the original y basis. (b) The same but away from the origin on the logarithmic scale. The (overlapping) plots for $y=1$ (the upper leg) and $y=2$ (the lower leg) are almost indiscernible. The parameters are set to $t_h'=0.345$, $g=0.1$, and $E_d=0.3$. The wave function is normalized such that $\psi_d=1$.

the self-energy can be seen as a general indicator for the QBIC phenomenon.

C. Other aspects of QBIC including wave function analysis, spectral weight, and the emerging QBIC

In this section we investigate more closely some additional properties of the QBIC. We will begin by looking more closely at the wave function for QBIC state Q2. In particular, we will show that the wave function for Q2 appears to be localized near $x=0$, although it actually behaves as a decaying state with an exponential divergence for large x. We will also verify that the − channel provides the dominant contribution to this wave function in the vicinity of the origin. This conforms to our expectations since it is the singularity associated with this channel that results in the nearly localized behavior of this state. (Note that we have added quotation marks on the minus sign above to avoid any confusion in the notation. Hereafter, we will drop the quotation marks and simply write this as − channel.) We will also compare the time evolution of the ordinary decaying state S1 with that of Q2 in order to demonstrate that the QBIC decays on a much more gradual time scale than an ordinary decaying state. We will then calculate the spectral weight of the QBIC as the residue of the Green's function. While the spectral weight of the ordinary QBIC will turn out to be small, the form of the residue function will lead us directly to the emerging QBIC, a state with reduced metastable properties, but significantly enhanced spectral weight.

1. Wave function for QBIC state Q2 in the $y=1,2$ basis

In Figs. 16(a) and 16(b) we plot a numerical result of the wave function from Eq. (17) in the nondiagonalized channels $y=1,2$ for state Q2. Looking at Fig. 16(a) (linear scale) we see that the wave function for Q2 appears to be localized for values of x near the origin (where the adatom is attached to the wire system). However, in Fig. 16(b) (logarithmic scale) we see that the wave function indeed behaves as that for a decaying state with an exponential divergence in space far away from the origin. Also notice that the contributions to the wave function from the two original channels $y=1,2$ are almost exactly equal in either plot (the two graphs are overlapping).

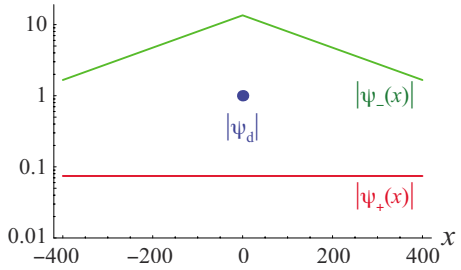

FIG. 17. (Color online) The eigenfunction of state Q2 in the σ basis for $t_h'=0.345$, $g=0.1$, and $E_d=0.3$ on a logarithmic scale as a function of position. The amplitude modulus of the − channel, $|\psi_-(x)|$, that of the + channel, $|\psi_+(x)|$, and that of the dot, $|\psi_d|$, are indicated. The wave function is normalized such that $\psi_d=1$.

2. Wave function for QBIC state Q2 in the $\sigma=+,-$ basis

In Fig. 17 we plot separately a numerical result of the wave function contribution to state Q2 from the + and − channels [as exemplified in Eq. (14)] in the basis of the partially diagonalized Hamiltonian (4). We also plot the discrete wave function associated with the impurity state, each at initial time $t=0$ with the usual choice of parameters $t_h'=0.345$, $g=0.1$, and $E_d=0.3$. Keeping in mind the numerical choice for the coupling constant $g=0.1$, we can see in this figure that at the origin the amplitude of the wave function $|\psi_-(x)|$ for state Q2 in the − channel is of the order g larger than that of the adatom wave function $|\psi_d|$ and that in turn $|\psi_d|$ is order g larger than the amplitude of the wave function $|\psi_+(x)|$ in the + channel. This implies that $|\psi_+(x)|$ is order g^2 smaller than $|\psi_-(x)|$, owing to the fact that the singularity in the − channel is responsible for the (dominant) localized behavior of the state near the origin.

We may analytically demonstrate the relative orders of the wave functions by making use of the results that we obtained for the QBIC state previously in Sec. II B. First we may add or subtract the first two equations in Eq. (18) to obtain

$$\frac{|\psi_d|}{|\psi_\pm(0)|} = \frac{\sqrt{2}t_h}{g}|\sin K_\pm| \tag{42}$$

and the *channel weight function*

$$\theta(E) \equiv \frac{|\psi_+(0)|}{|\psi_-(0)|} = \frac{|\sin K_-|}{|\sin K_+|} = \frac{\sqrt{t_h^2-(E-t_h')^2}}{\sqrt{t_h^2-(E+t_h')^2}}, \tag{43}$$

in which we have made use of Eq. (13) to write $\psi_\pm(0)=A_\pm$ at the origin $x=0$. These relations hold for any of the 12 eigenstates of the ladder system.

Let us evaluate this function for QBIC state Q2. We here use the relations for the QBIC eigenvalue $E=E_{Q2}$ and the corresponding wave numbers $K_\pm$. We can now use expansion (41) with Eq. (7) to obtain

$$\sin K_+ = 2\sqrt{\frac{t_h'}{t_h}\left(1-\frac{t_h'}{t_h}\right)} + O(g^4) \tag{44}$$

and

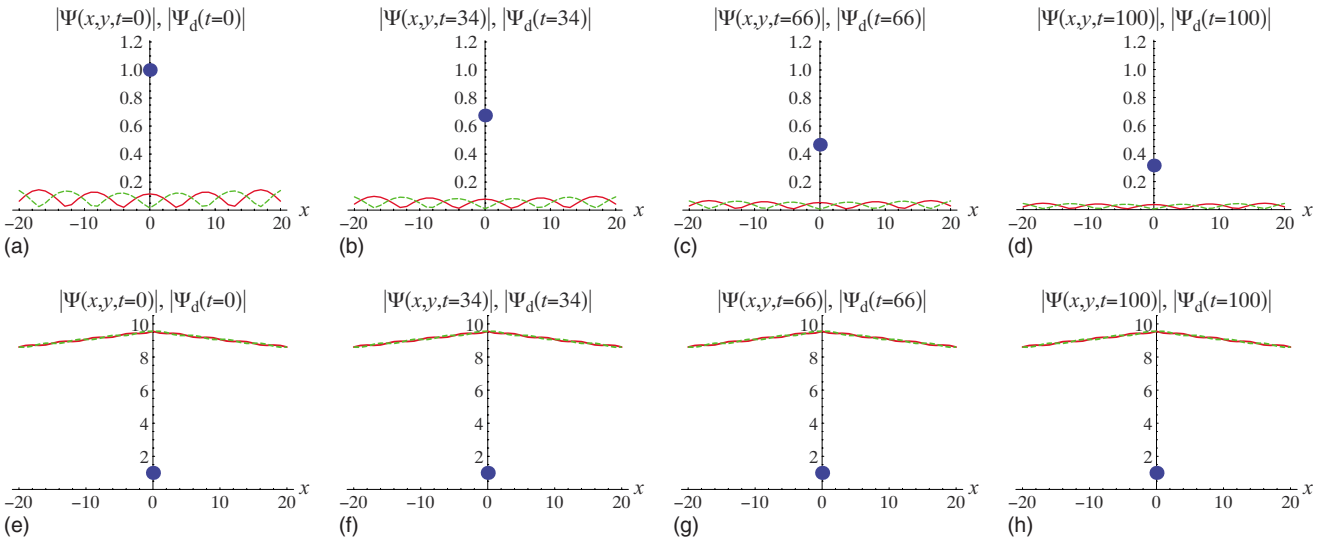

FIG. 18. (Color online) Time evolution of wave function for solutions [(a)–(d)] S1 and [(e)–(h)] Q2 for $t_h'=0.345$, $g=0.1$, and $E_d=0.3$. The solid (red) curves represent $\Psi(x,1,t)$, the broken (green) curves represent $\Psi(x,2,t)$, and the dots represent $\Psi_d(t)$. The wave functions are normalized such that $\Psi_d(0)=1$. The QBIC solution Q2 clearly decays on a much slower time scale than that of the ordinary decay state S1.

$$\sin K_- = i\frac{1}{2t_h(t_h' - t_h - E_d)}g^2 + O(g^4). \tag{45}$$

Applying these in Eq. (42) gives

$$\frac{|\psi_d|}{|\psi_\pm(0)|} \sim g^{\mp 1}, \tag{46}$$

in agreement with our discussion of Fig. 17 above. Finally, the channel weight function [Eq. (43)] for state Q2 is given by

$$\theta(E_{Q2}) = \frac{|\psi_+(0)|}{|\psi_-(0)|} = \frac{g^2 t_h^2}{4\sqrt{t_h'(t_h - t_h')}|- t_h + t_h' - E_d|}, \tag{47}$$

such that the contribution of the + channel is order g^2 smaller than that of the − channel.

3. Generic channel weight function

As mentioned, we may generalize the preceding discussion to states other than Q2. As an application of Eq. (43), consider the decaying states S1 and Q2 in the vicinity of the *outer* band edge at $-t_h - t_h'$. Here state Q2 will not behave as a QBIC state with a small decay rate but instead has an amplified decay rate of order $g^{4/3}$ in the vicinity of the singularity at the outer band edge [for example, see Fig. 11(a)].[2] State S1 also has an amplified decay rate for this range $E_d \sim -t_h - t_h'$. For either of these solutions, Eq. (43) gives $\theta(E_{S1,Q2}) \sim g^{-2/3}$, demonstrating that in this case, it is the lower channel + that provides the largest contribution to the wave function. The reason for this is that it is the van Hove singularity at the outer band edge $-t_h - t_h'$ (associated with the lower band edge E_+) that results in the amplification of the decay rate, while the upper channel E_- plays little role in this effect in this region of the energy spectrum.

4. Time evolution for QBIC state Q2 against ordinary decaying state S1

In Fig. 18 we show the time evolution $\Psi(x,y,t)$ and $\Psi_d(t)$ for states S1 and Q2 for the choice of the parameters $t_h' = 0.345t_h$, $g=0.1t_h$, and $E_d=0.3t_h$, under which state Q2 will behave as a QBIC state. We see that indeed on the time scale under which the ordinary state S1 decays almost completely, state Q2 appears to behave as a localized state without a noticeable decay rate (for this time scale). The details of the numerical method by which we have obtained the time-evolution simulations in these plots are presented in Appendix.

5. Spectral weight of QBIC state

Up to this point, we have primarily characterized the system by the eigenvalues of the dispersion equation [Eq. (11)], that is, the poles of the Green's function. However, we can also characterize the poles by the residues of the Green's function, which is interpreted as the spectral weight for each pole.[39] Our goal will be to compare the spectral weight of the QBIC state with that of the ordinary decaying state that obeys Fermi's golden rule. Since we have developed a straightforward method for generating perturbative approximations for each of the poles (as in Sec. III B 2), it is easy to write a generic formula useful for obtaining analytic approximations for the residue of the pole. We obtain this formula as

$$\mathrm{Res}[G_{dd}(z_0)] = \lim_{z\to z_0}(z - z_0)G_{dd}(z) = r(z_0), \tag{48}$$

in which we obtain the residue function $r(z_0)$ through

$$[r(z_0)]^{-1} \equiv 1 + \frac{g^2}{2}\left\{\pm\frac{z_0 + t_h'}{[(z_0 + t_h')^2 - t_h^2]^{3/2}} \pm \frac{z_0 - t_h'}{[(z_0 - t_h')^2 - t_h^2]^{3/2}}\right\}. \tag{49}$$

This relation is determined by application of L'Hôpital's rule.

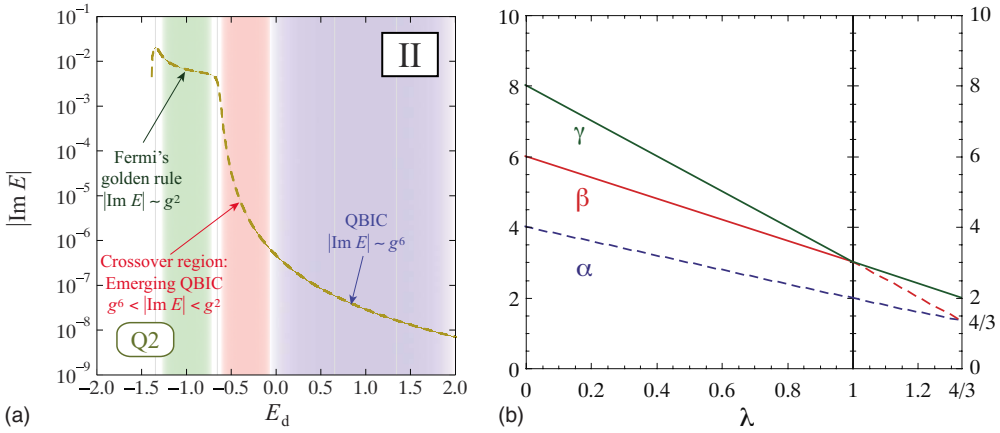

FIG. 19. (Color online) (a) Same as Fig. 11(b) but with the crossover region $g^{4/3} < E_d - (-t_h + t_h') < g^0$ indicated by light red shading. For this region with values of the impurity energy $E_d \gtrsim -t_h + t_h'$ that are above but near the lower inner band edge, we have an intermediate behavior where the decay rate for Q2 becomes metastable with $g^6 < \mathrm{Im}\,E < g^2$ but has not yet become a full QBIC state with $\mathrm{Im}\,E \sim g^6$. We refer to this as the emerging QBIC. (b) The dependence of the exponents α, β, and γ in expansion (35) on the exponent λ in Eq. (51). The broken lines indicate that the expansion terms have real coefficients. The expansion terms indicated by the solid lines have complex coefficients, which result in the decay rate.

The signs $\pm$ in $R(z_0)$ are associated with the Riemann sheets of the complex energy surface and must be chosen correctly for the appropriate sheet for a given solution (keep in mind that the signs can change within a single sheet in the energy representation). While $r(z_0)$ is the exact residue in the above form, we will use it below as a convenient shorthand for writing analytic approximations.

It is now simple to obtain the residues for the ordinary decaying state S1 and QBIC state Q2 for comparison. Let us assume the impurity energy E_d lies in the vicinity of the middle of the spectrum, well inside the two inner band edges. In this portion of the spectrum, state S1 can be approximately described by Fermi's golden rule, with the behavior $E_{S2} \approx E_d + \chi g^2$, with χ order unity as usual. Then to lowest order the residue is given simply by $\mathrm{Res}[G(E_{S2})] \approx r(E_d) \sim 1 + O(g^2)$. Here we must choose the sign combination $(-,+)$ as can be shown to be appropriate for sheet IV in the middle of the spectrum.

The residue for QBIC state Q2 can then be easily obtained by plugging in our perturbative result for the eigenvalue E_{Q2} as given in Eq. (41) into $r(z_0)$. In this manner we obtain

$$\mathrm{Res}[G_{dd}(E_{Q2})] \approx \frac{g^4}{4t_h(t_h' - t_h - E_d)^3} \tag{50}$$

such that $\mathrm{Res}[G(E_{Q2})] \sim g^4$.

Clearly, this gives the Q2 state a significantly smaller spectral weight, which indicates that experimental detection might prove challenging. However, notice that the denominator of this result may provide a way to avoid this problem. It is clear that when the impurity energy E_d lies near to the band edge $t_h' - t_h$ then the spectral weight of the QBIC state in Eq. (50) will be dramatically amplified. Of course, our assumption when we derived an approximation for the QBIC state in Sec. III B 2 was that $E_d \gg -t_h + t_h'$, which gives us pause. Fortunately, we will be able to show in Sec. III C 6 below that state Q2 is still metastable in this "crossover" region $E_d \gtrsim -t_h + t_h'$ with a decay rate that is smaller than the ordinary g^2 but larger than the "full" QBIC decay rate g^6.

Since this state has the characteristics but not yet the full decay rate of the QBIC state, we will refer to this as the *emerging QBIC* state. We will then refer to the portion of the spectrum in which the emerging QBIC appears as the *crossover region*. The concept of the crossover region will again prove useful when we consider in greater detail the decay rate amplification near the van Hove singularity in Sec. IV A.

6. Emerging QBIC

As discussed in Sec. III C 5, we now consider in greater detail the decay rate of the emerging QBIC state in the crossover region in which the impurity energy lies in the vicinity of (but not too near to) one of the inner band edges; we will be more precise about this statement momentarily. In Sec. IIB2 we obtained an approximation for the decay rate of QBIC state Q2 in the region $E_d \gg -t_h + t_h'$. In the present section our region of interest will be $E_d \gtrsim -t_h + t_h'$. In this region we will find a metastable state with a decay rate that is larger than the QBIC decay rate g^6 but smaller than the ordinary decay rate g^2. Hence we will refer to this as the emerging QBIC state. Meanwhile we will refer to this region inside but near the inner band edge ($E_d \gtrsim -t_h + t_h'$ for Q2) as the crossover region. We depict these regions for Q2 in the semilogarithmic plot in Fig. 19(a). The crossover region is indicated with red shading in this figure. While the decay rate of the emerging QBIC is not yet as small as that for the full QBIC, it is clear from Eq. (50) that the spectral weight of this state will be amplified relative to the full QBIC. This should render the emerging QBIC easier to detect experimentally, for example, by STM probe as will be explored further in Sec. IV B below.

In order to study the emerging QBIC state Q2 in the crossover region, let us reparametrize the discrete energy in terms of its proximity to the inner band edge $-t_h + t_h'$ according to

$$E_d \equiv (-t_h + t_h') + E_\lambda g^\lambda. \tag{51}$$

Here E_λ is some number of order unity. Hence, this expression measures distance from the inner band edge in terms of the order of λ in g^λ. When $\lambda=0$ we are deep inside the overlapping region between the bands where the QBIC is described by Eq. (41), while $\lambda>0$ brings us closer to the inner band edge $-t_h+t_h'$. By inspection we will find that when $\lambda=4/3$ the amplification effects from the van Hove singularity reassert themselves. Hence the crossover region can be quantitatively defined in terms of Eq. (51) as the portion of the spectrum for which $0<\lambda<4/3$.

We will find below that it is necessary to further subdivide the crossover region into a far zone $(0<\lambda<1)$ and a near zone $(1<\lambda<4/3)$. Here "nearness" refers to the proximity of E_d to the inner band edge $-t_h+t_h'$. We will show below that in the far zone the eigenvalue expansion for Q2 is given by

$$E_{Q2} = (-t_h + t_h') - \frac{1}{8t_h E_\lambda^2} g^{4-2\lambda} - i\frac{1}{16t_h E_\lambda^3 \sqrt{t_h'(t_h - t_h')}} g^{6-3\lambda} + O(g^{8-5\lambda}) \quad (0<\lambda<1) \tag{52}$$

with the emerging QBIC decay rate appearing as the second-lowest-order term proportional to $g^{6-3\lambda}$. Meanwhile, in the near zone we will instead obtain

$$E_{Q2} = (-t_h + t_h') - \frac{1}{8t_h E_\lambda^2} g^{4-2\lambda} - \frac{1}{32 t_h^2 E_\lambda^5} g^{8-5\lambda} + O(g^{6-3\lambda}) \quad (1<\lambda<4/3), \tag{53}$$

in which the emerging QBIC decay rate only appears as the third-lowest-order correction term (the fourth term on the RHS). Notice that still this term is proportional to $g^{6-3\lambda}$, as in the far zone. Hence the order of the decay rate is actually continuous across the two zones. The remainder of this section is dedicated to obtaining these two results. The reader who is primarily interested in the physical and experimental implications of these results (rather than their derivation) may proceed directly to Sec. IV.

In order to obtain Eqs. (52) and (53) let us apply our familiar expansion for the QBIC eigenenergy, as given in Eq. (35), to the dispersion equation [Eq. (11)] and expand to obtain

$$\begin{aligned} -E_\lambda g^\lambda + \chi_\alpha g^\alpha + \chi_\beta g^\beta + \chi_\gamma g^\gamma &\approx \left(\frac{g^{2-\alpha/2}}{2\sqrt{-2t_h\chi_\alpha}} - \frac{\chi_\beta g^{\beta-\alpha+(2-\alpha/2)}}{4\sqrt{-2t_h\chi_\alpha^3}} + g^{2-\alpha/2} O(g^{\gamma-\alpha}, g^\alpha, g^{2(\beta-\alpha)}) \right) \\ &\quad + \left(\frac{g^2}{2\sqrt{(2t_h'-t_h)^2 - t_h^2}} + O(g^{\alpha+2}) \right). \end{aligned} \tag{54}$$

This expression of course is quite similar to expansion (36), which we obtained for the full QBIC at $\lambda=0$; we recover the earlier expression with the simple substitution $E_\lambda g^\lambda = E_d - (-t_h+t_h')$.

Throughout the crossover region $0<\lambda<4/3$, the lowest-order correction is obtained by equating the first term in the first set of parentheses on the RHS with the first term on the LHS according to

$$-E_\lambda g^\lambda = \frac{g^{2-\alpha/2}}{2\sqrt{-2t_h\chi_\alpha}}. \tag{55}$$

This is actually the same lowest-order condition (with slightly different notations) as in the full QBIC case, given in Eq. (36). From Eq. (55) we have the condition on α as $\alpha=4-2\lambda$ for the emerging QBIC state. Notice that $\alpha\to4$ as $\lambda\to0$, which shows that this lowest-order result then reduces to the earlier result for the full QBIC [Eq. (41)]. We can also now obtain the condition on χ_α, given explicitly below.

Meanwhile, for the second-lowest-order condition we should take some extra care. In the far zone of the crossover region $(0<\lambda<1)$ we can obtain the second-lowest-order correction for the emerging QBIC in the same manner as we did for the full QBIC. That is, by equating the second term in the first set of parentheses on the RHS with the g^2 order term in the second set of parentheses,

$$\frac{\chi_\beta g^{\beta-\alpha+(2-\alpha/2)}}{4\sqrt{-2t_h\chi_\alpha^3}} = \frac{g^2}{2\sqrt{(2t_h'-t_h)^2 - t_h^2}}. \tag{56}$$

This gives us the second-lowest-order condition on β as $\beta=3\alpha/2=6-3\lambda$. As before, this term represents the interaction between the singularity in one band with the continuum of the other and hence yields the appearance of the metastable decay rate. Indeed, this second-lowest-order correction yields the full QBIC decay rate g^6 as $\beta\to6$ for $\lambda\to0$. Finally, we equate the next order terms as

$$\chi_\alpha g^\alpha = g^{2-\alpha/2} O(g^{\gamma-\alpha}), \tag{57}$$

giving $\gamma=8-5\lambda$. Thus, after collecting our results up to this point, we can write the expression for the emerging QBIC in the far zone as reported above in Eq. (52). Clearly this reduces to the previous expression [Eq. (41)] for the QBIC in the limit $\lambda\to0$.

However, a problem occurs in the above argument when $\lambda>1$. Notice at $\lambda=1$, the order of the $g^{6-3\lambda}$ term and that of the $g^{8-5\lambda}$ term in Eq. (52) will meet at $6-3\lambda=8-5\lambda=3$, as indicated in Fig. 19(b). This indicates that at this point, the second-lowest-order correction (β) and third-lowest-order correction (γ) switch roles. Curiously, the lowest order of the decay rate itself is actually continuous across this transition, as mentioned above.

Let us examine the $\lambda>1$ case in greater detail. At this point $\alpha=4-2\lambda<2$ such that the $\chi_\alpha g^\alpha$ term on the LHS of our expansion (54) will now dominate over the g^2 term in the second set of parentheses on the RHS. Hence, for the near zone of the crossover region $1<\lambda<4/3$ we must obtain the second-lowest-order correction by equating the second term in the set of parentheses on the RHS with the g^α order term instead of the g^2 term,

$$\chi_\alpha g^\alpha = -\frac{\chi_\beta g^{\beta-\alpha+(2-\alpha/2)}}{4\sqrt{-2t_h\chi_\alpha^3}}. \tag{58}$$

This is opposed to the preceding case of the far zone in which the $g^{\beta-\alpha+(2-\alpha/2)}$ term (associated with the embedded singularity) was equated with the g^2 term (associated with the embedding channel) as in Eq. (56), yielding the QBIC decay rate $\beta=6-3\lambda$. In the present case, this second-lowest-order contribution yields a purely real contribution to the eigenvalue of order $\beta=5\alpha/2-2=8-5\lambda$. Meanwhile, the QBIC effect in this case results instead from the interaction of the $g^{\gamma-\alpha+(2-\alpha/2)}$ term in the first set of parentheses on the RHS with the g^2 term in the second set of parentheses on the same side,

$$\frac{g^2}{2\sqrt{(2t_h'-t_h)^2-t_h^2}} = g^{2-\alpha/2}O(g^{\gamma-\alpha}). \tag{59}$$

This again results in a QBIC decay rate of order $\gamma=6-3\lambda$ in the region $1<\lambda<4/3$, although now appearing only at third-lowest-order perturbation theory as reported above in Eq. (53). In the limit $\lambda=1$ we have $\alpha=2$ and $\beta=\gamma=3$, while in the limit $\lambda=4/3$ we have $\alpha=\beta=4/3$ and $\gamma=2$. The dependence of these exponents α, β, and γ on λ is summarized in Fig. 19(b). We emphasize that the exponent for the decay rate varies as $6-3\lambda$ throughout the crossover region.

IV. DECAY RATE AMPLIFICATION IN THE CROSSOVER REGION AND THE LOCAL DENSITY OF STATES PROFILE

In this section we will study the presence of various effects in the system, each of which will be, directly or indirectly, a result of the divergent DOS singularities. Note that the first topic we will consider in this section (decay rate amplification near the DOS singularity) may at first glance seem like a departure from our main topic, which is the QBIC. However, the results given in Sec. IV A below will be helpful to us in our understanding of the Fano effect in the local density of states in Sec. IV B. Further, we will find that the Fano effect gives the most apparent candidate for experimental detection of the QBIC. Hence, while we will begin this section by studying a different type of effect from the van Hove singularity, we will gradually work our way back to the QBIC phenomenon.

In Sec. III C 6 we investigated the behavior of the emerging QBIC in the crossover region. We will begin our studies of the $g^{4/3}$ decay rate amplification by conducting a similar investigation for state S1. We will show that a similar crossover behavior occurs between the region near the singularities and the region far away from them where Fermi's golden rule holds. In fact, the region of the energy spectrum where this crossover behavior occurs is precisely the same as that for the emerging QBIC. This of course is because both effects are a result of the divergent DOS singularity.

We will then present some results of the local density of states (LDOS) calculation that describes the probability for electron localization at the impurity site as a function of energy. This can potentially be used as a means to probe the discrete eigenstates at a given impurity energy E_d by means of scanning tunneling microscopy (STM). We will first show that when the impurity energy lies in the vicinity of one of the inner band edges, the presence of two strongly amplified resonant states (due to the singularity) and one resonant state with a smaller decay rate results in an asymmetric LDOS profile. This is characteristic of the Fano interference between discrete states.[28,29] Finally we will show the LDOS profile in the crossover region, focusing our attention on the emerging QBIC state for the $\lambda=1$ case discussed in Sec. III C 6. We will see graphically in this case that the emerging QBIC is indeed a strong feature in the system, owing in part to the Fano effect. Hence this may well provide the best chances for experimental detection of the QBIC.

A. Amplification of the decay rate due to the van Hove singularity

As we discussed in Sec. III A, the decay rate for certain states is amplified in the vicinity of the divergent band-edge singularities, such as state S1; state S1 is the one state that is actually amplified at all four of them. This effect is not unique to the present system, but it is quite ubiquitous among systems that are closed in all but one dimension, having an energy continuum (or continua) with a cutoff value. When an excited discrete state is coupled with the continuum near the cutoff, Fermi's golden rule breaks down. In most cases this results in a characteristic $g^{4/3}$ amplification of the decay rate. This has been presented previously for a two-level oscillator coupled with the field modes inside an electromagnetic waveguide[5] and a single-channel quantum wire with an adatom impurity,[2] similar to the situation for the S1 state discussed above.

In order to facilitate later discussion of the Fano effect in the local density of states calculation we will now consider this point in greater detail. First we will write an analytic approximation for the $g^{4/3}$ decay rate near where the maximum value is realized and reiterate the conditions under which this effect should occur. Then we will present another approximation that describes the decay rate as the system transitions between the region where Fermi's golden rule holds and the region where the $g^{4/3}$ "rule" is obeyed. We will use state S1 as our prototype throughout this discussion, but we will obtain useful results for other states as a by-product of our development.

From previous work, we know that for these types of one-dimensional systems the van Hove singularity provides maximum decay rate amplification in a quite specific domain of the energy spectrum. If we assume that there is a divergent van Hove singularity at band edge W, then to lowest order the decay rate will be proportional to $g^{4/3}$ when the energy of the discrete state E_d is within the range $|E_d-W|\lesssim O(g^{4/3})$. Hence we will refer to this region as the $g^{4/3}$ *amplification region*. The maximum itself tends to occur near the actual value $E_d=W$.

1. General characteristics of the $g^{4/3}$ amplification

In the present case of the two-channel quantum wire model, let us focus on the region $|E_d-(-t_h+t_h')|\lesssim O(g^{4/3})$

around the lower inner band edge. Notice that this is the region depicted in closeup Fig. 8(f). Here we see the real parts of the eigenvalue for six solutions. It is conceptually useful for us to divide these into three pairs of conjugate solutions, (Q2;Q3), (S1;S2), and (RQ5;RQ4). Notice that we have paired these solutions in the format (decay;growth solution). Also notice that the real values of these solutions [y axis in Fig. 8(f)] all lie close to the lower inner band edge $-t_h+t_h'=-0.655$ [horizontal gray line in Fig. 8(f)]. We emphasize that in this region state Q2 is *not* a QBIC state. As we will see below, each of these six solutions undergoes the characteristic $g^{4/3}$ behavior due to the divergent singularity at the lower inner band edge. However, there is one subtlety in this case: the $g^{4/3}$ behavior *only affects the energy shift for the conjugate pair* (Q2;Q3). Hence the decay rate for solution Q2 in this region only appears at second-lowest-order perturbation theory. Somewhat ironically, this results in a decay rate of order g^2 for Q2. However, we emphasize that this result is not related to the Fermi golden rule, as the golden rule always breaks down in the vicinity of the DOS singularity. The discrepancy in the magnitude of the decay rates of Q2 ($\gamma\sim g^2$) and S1/RQ5 ($\gamma\sim g^{4/3}$) will result directly in the Fano effect discussed below in Sec. IV B.

We will choose to perform our perturbation calculation at the exact point $E_d=-t_h+t_h'$, which is given by the vertical gray line in Fig. 8(f). Here we will find that the calculation will simplify. This point lies also near to that where the maximum decay rate amplification occurs and will serve well as a representative of the entire portion of the spectrum $|E_d-(-t_h+t_h')|\lesssim O(g^{4/3})$. Before we undertake the calculation, let us make a few notes on what we expect to find. First, note in Fig. 8(f) that the real parts of the conjugate pairs (S1;S2) and (RQ5;RQ4) lie very close together; they are indistinguishable at the point of intersection with the vertical gray line. This is an indication that the energy shifts (real parts of the eigenvalues) for each of these four solutions are equal up to first-lowest order. This will be confirmed by our calculation. Also notice that these four solutions are shifted upward from the band edge (horizontal gray line). Meanwhile the energy shift for the conjugate pair (Q2;Q3) is downward and is slightly larger than that for the other four solutions. Finally, notice in Figs. 9(b)–9(d) that at the lower inner band edge (second vertical gray line from the left in each graph) the complex part of the eigenvalue for the pair (Q2;Q3) in Fig. 9(b) is much smaller than that for the other two pairs (RQ5;RQ4) and (S1;S2) in Figs. 9(c) and 9(d), respectively. This is consistent with our statement above that S1 and RQ5 will exhibit the $g^{4/3}$ decay resulting from the singularity, while Q2 will have a smaller decay rate of order g^2. Finally, we note that between the pairs (S1;S2) and (RQ5;RQ4), the former has a slightly larger complex part of the eigenvalue than the latter. This will also come out of our calculation.

In order to perform the actual calculation, we make the usual type of expansion $E_X=(-t_h+t_h')+\chi_\alpha g^\alpha+\chi_\beta g^\beta+\ldots$ for the eigenvalue. Here X may be any of the six solutions discussed above. (Of course, in the end we are primarily interested in the three decay solutions S1, RQ5, and Q2.) Notice that in the above expansion, we are assuming that each of the six solutions has an equal (purely real) eigenvalue at the lowest order. That is, $E_X=E^{(0)}+O(g^\alpha)$ with $E^{(0)}=-t_h+t_h'$ for each solution X. We will find below that including the first-lowest-order term in this expansion (order α) allows us to divide the solutions into three pairs, although we must emphasize that *these pairings are not the same as the pairings of the type* (decay;growth). Instead, the solutions will be paired according to the magnitude of the imaginary part of the complex eigenvalue. Hence, Q2 and Q3 will be paired as the solutions with the smaller imaginary part of the eigenvalue (these solutions are real to first-lowest order). Likewise, S1 and RQ5 will be paired as the two decaying solutions that experience the $g^{4/3}$ amplification of the decay rate and finally S2 and RQ4 are paired as the growth solutions that experience complex $g^{4/3}$ amplification as well.

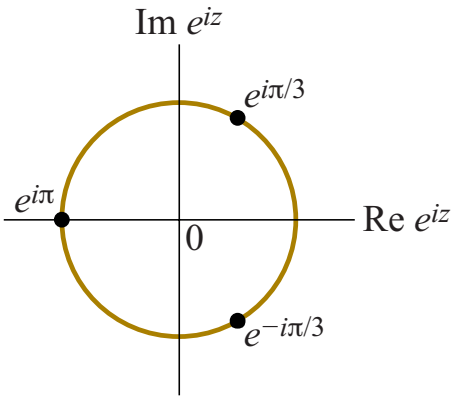

FIG. 20. (Color online) The cubic roots of $e^{i\pi}=-1$ on the unit circle. The three roots are given by $e^{\pm i\pi/3}$ and $e^{i\pi}$ itself.

Plugging our expansion for E_X into the discrete dispersion equation [Eq. (11)], we obtain an expansion equivalent to that in Eq. (36) except that the term on the LHS in parentheses vanishes (this occurs because we chose $E_d=-t_h+t_h'$). Among the terms remaining in Eq. (36), it can be shown that the only consistent choice is to equate the following sets of terms:

$$\chi_\alpha g^\alpha = \frac{g^{2-\alpha/2}}{2\sqrt{-2t_h\chi_\alpha}}, \tag{60}$$

$$\chi_\beta g^\beta = -\frac{\chi_\beta g^{\beta-\alpha+(2-\alpha/2)}}{4\sqrt{-2t_h\chi_\alpha^3}} + \frac{g^2}{2\sqrt{(2t_h'-t_h)^2-t_h^2}}, \tag{61}$$

$$\chi_\gamma g^\gamma = g^{2-\alpha/2}O(g^{\gamma-\alpha},g^\alpha). \tag{62}$$

We will now consider each of these conditions in turn.

Let us consider the first-lowest-order term in Eq. (60). It is easy to obtain the expected order $\alpha=4/3$ from $\alpha=2-\alpha/2$. After dividing out the g factor on both sides of this equation, we can obtain the condition on the coefficient χ_α as $\chi_\alpha^3=-1/8t_h$. When taking the cubic root to find χ_α, we must take care that we use each of the three complex roots. It is most straightforward to "absorb" the complex factor in this relation into the negative sign by writing $-1=e^{i\pi}$. Then we have

$$\chi_\alpha = 1/2t_h^{1/3}(e^{i\pi})^{1/3}, \tag{63}$$

with $t_h^{1/3}$ now just the ordinary real cubic root of the real number t_h. We can then obtain the three complex cubic roots as $(e^{i\pi})^{1/3}=e^{i\pi}$ or $e^{\pm i\pi/3}$. We show these three roots on the unit circle in the complex plane in Fig. 20. Notice that the first root $e^{i\pi}=-1$ is purely real, while the other two roots $e^{\pm i\pi/3}=(1\pm i\sqrt{3})/2$ are complex conjugates with equal (positive) real part. The first root gives the first-order correction for the conjugate pair (Q2;Q3), which are both real to order $\alpha=4/3$. This tells us that the energy shift *alone* experiences the $g^{4/3}$ amplification from the DOS singularity for these two solutions. These solutions have a shared value $\chi_\alpha^{Q2,Q3}=-1/2t_h^{1/3}$. This leaves the decay rate of solution Q2 "untouched" by the singularity at this order.

The two remaining roots $e^{\pm i\pi/3}$ are associated with the four remaining solutions S1, S2, RQ4, and RQ5, which are shifted upward from $y=E_d$ in Fig. 8(f) and experience the $g^{4/3}$ decay in Figs. 9(c) and 9(d). Clearly the root $e^{-i\pi/3}=(1-i\sqrt{3})/2$ is associated with the two decaying solutions S1 and RQ5. Since the imaginary part of this root is nonzero, we see instantly that the lowest order of the decay rate appears at order $g^{4/3}$, conforming to our expectations. Also notice that the energy shift for these two solutions is positive, whereas the energy shift for the pair (Q2;Q3) was negative. This agrees with the graph in Fig. 8(f). Hence we have the shared value $\chi_\alpha^{S1,RQ5}=1/2t_h^{1/3}e^{-i\pi/3}$ for the decaying solutions S1 and RQ5, which are degenerate to first-lowest order. Finally, we have the remaining root $e^{i\pi/3}=(1+i\sqrt{3})/2$ that gives the conjugate growth partners S2 and RQ4, with $\chi_\alpha^{S2,RQ4}=1/2t_h^{1/3}e^{i\pi/3}$.

In Fig. 21(a) we (qualitatively) represent the transition from the lowest-order to the first-lowest-order perturbation result. In this figure the brown curve represents a circle of radius $|\chi_\alpha|=|1/2t_h^{1/3}|$ in a displaced version of the complex plane. Here we have displaced the origin so that the real axis originates at the lower inner band edge $-t_h+t_h'$. In other words, the origin of this plot is exactly the lowest-order result $E^{(0)}$ for all six of the eigenvalues presently under consideration. This lowest-order result is shown as the red point at the origin. The green arrows then represent the magnitude and direction of the three values of χ_α as vectors in the complex plane. These vectors indicate the transition to the first-lowest-order results for the eigenvalues. The blue dots represent the three pairs that are degenerate up to this order of approximation (for example, we have $E_{Q2,Q3}^{(\alpha)}=E^{(0)}+\chi_\alpha^{Q2,Q3}g^{4/3}$). This diagram should be considered qualitative only, with g effectively set equal to unity.

Turning to the second-lowest-order condition [Eq. (61)], we can use $2-\alpha/2=\alpha=4/3$ to obtain the order of the correction β immediately. For each of the three respective terms we have $\beta=\beta-\alpha+\alpha=2$. We also notice immediately that χ_α itself does not appear in Eq. (61). Instead, only $\chi_\alpha^3=-1/8t_h$ appears, which is equal for each of the three first-order pairings (in other words, all six solutions). This implies that a given pairing will have the same value of χ_β as the other two pairings, but we will see that χ_β has two values, which will introduce a splitting in each individual pair. Explicitly solving for χ_β gives a purely imaginary second-lowest-order correction according to

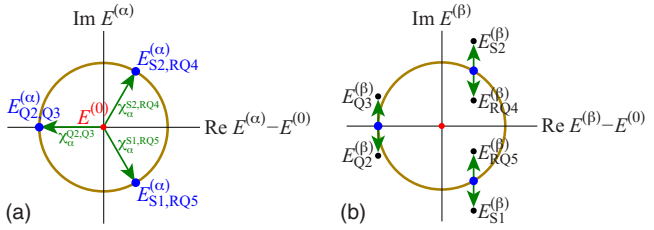

FIG. 21. (Color online) Qualitative diagrams depicting the transitions from lowest-order correction (one red point) to first-lowest-order correction (three blue points) and then to second-lowest-order correction (six black points) in the perturbation calculation for the three conjugate pairs of solutions, (Q2;Q3), (S1;S2), and (RQ5;RQ4), at the value $E_d=-t_h+t_h'$ (inner lower band edge). (a) Transition from lowest-order correction to first-lowest-order correction. The brown circle represents a circle of radius $|\chi_\alpha|=|1/2t_h^{1/3}|$ (with $g=1$ for simplicity). The origin has been offset so that the real axis is centered on the lower inner band edge $-t_h+t_h'$, which is the zeroth-order approximation for each of the six states. The zeroth-order approximation $E^{(0)}=-t_h+t_h'$ is labeled in red. The green arrows indicate the magnitude and direction of the three values of χ_α. These arrows represent the transition to the first-lowest-order approximation, in which the solutions are divided into three pairs. The first-lowest-order values of Q2 and Q3 (purely real to first order), S2 and RQ4 (two of the growth solutions), as well as S1 and RQ5 (two of the decaying solutions) are given as blue points on the circle. (b) Transition from first-lowest-order correction to second-lowest-order correction. At second-lowest order the three pairs of solutions are split into six distinct solutions, each labeled in black. Only at this level does the complex part of the eigenvalue appear for the conjugate pair of solutions (Q2;Q3), separating them into two distinct solutions. It is also at this level that the pair of solutions (S1;S2) becomes distinct from the pair (RQ5;RQ4). In this diagram, the green arrows pointing up represent the positive value for χ_β in Eq. (64) and the arrows pointing down represent the negative value.

$$\chi_\beta = \pm \frac{i}{6\sqrt{t_h'(t_h-t_h')}}. \tag{64}$$

We see that this second-order correction provides for splitting among the solutions that were paired at first-lowest order. This splitting is represented by the green arrows in Fig. 21(b), with the up arrows representing the positive value of Eq. (64) and the down arrows representing the negative value.

For example, the pairing (Q2;Q3), which were purely real at first-lowest order, are now split into a decaying solution Q2, which takes the negative sign in Eq. (64), and a growth solution Q3, which takes the positive sign. Meanwhile, the other two first-lowest-order pairings are also split. Consider the decaying solutions S1 and RQ5. Since they were already complex solutions at order $g^{4/3}$ with equal decay rates (negative imaginary parts of the eigenvalue), they are now split at order g^2 into S1 [taking the negative sign in Eq. (64)] with the largest decay rate and RQ5 (taking the positive sign) with a slightly smaller decay rate. In other words, the decay rate for S1 grows slightly larger at second-lowest order and that

for RQ5 is slightly reduced. This is consistent with our expectations from Figs. 9(c) and 9(d), in which it is clear that S1 has the larger decay rate in this region. A similar consideration applies to the solutions S2 and RQ4 that are growth partners to S1 and RQ5, respectively.

In the end we have

$$\chi_\beta^{\mathrm{Q2}} = \chi_\beta^{\mathrm{S1}} = \chi_\beta^{\mathrm{RQ5}} = -\frac{i}{6\sqrt{t_h'(t_h - t_h')}} \tag{65}$$

for the three decaying solutions and

$$\chi_\beta^{\mathrm{Q3}} = \chi_\beta^{\mathrm{S2}} = \chi_\beta^{\mathrm{RQ4}} = \frac{i}{6\sqrt{t_h'(t_h - t_h')}} \tag{66}$$

for their respective growth partners. The transition from the first-lowest-order correction to the second-lowest-order correction is again demonstrated by the green arrows in Fig. 21(b). This demonstrates how the first-lowest-order pairings (three blue dots) are split into six distinct solutions at second-lowest order (black dots), all of which are now complex. The six distinct solutions X at second-lowest order (order β) are represented in this diagram as $E_X^{(\beta)}$.

Finally, we can easily obtain the order of the third-lowest-order correction from Eq. (62) as $\gamma = 2\alpha = 8$. We may now collect our results for each order to write the perturbative expansion for the three decaying solutions E_X as

$$E_{\mathrm{S1,RQ5}} = (-t_h + t_h') + \frac{1}{2t_h^{1/3}} e^{-i\pi/3} g^{4/3} \mp i \frac{g^2}{6\sqrt{t_h'(t_h - t_h')}} + O(g^{8/3}) \tag{67}$$

and

$$E_{\mathrm{Q2}} = (-t_h + t_h') - \frac{1}{2t_h^{1/3}} g^{4/3} - i \frac{g^2}{6\sqrt{t_h'(t_h - t_h')}} + O(g^{8/3}). \tag{68}$$

We emphasize here the difference in the magnitude of the decay rate between S1 and RQ5 on the one hand (both have $\gamma \sim g^{4/3}$) and Q2 on the other ($\gamma \sim g^2$). We will see in Sec. IV B that this discrepancy in the decay rates results in the asymmetric Fano effect in the local density of states calculation.

As we have discussed throughout the text, the $g^{4/3}$ effect is fairly ubiquitous for systems in which a discrete state is coupled near the van Hove singularity at the cutoff of a one-dimensional continuum. The general requirements then for the presence of the $g^{4/3}$ effect have been stated in Eq. (34), equivalent to the conditions for the presence of the persistent stable state, apart from the question of which region of the spectrum these effects occur. The decay rate amplification occurs in the region $|E_d - W| \lesssim O(g^{4/3})$, while the persistent stable state occurs for $|E_d - W| \gtrsim O(g^0)$.

2. Decay rate amplification in the crossover region

Now we consider more closely how the decay rate for a state such as S1 behaves as it transitions between the region where Fermi's golden rule holds and the $g^{4/3}$ amplification region. We will refer to the former as the *Fermi region*. The crossover region between the Fermi region and the $g^{4/3}$ region happens to be equivalent to the crossover region that we discussed in Sec. III C 6 for the QBIC (meaning that the crossover region for both effects occupies the same portion of the energy spectra). In the Fermi region the decay rate is proportional to the square of the coupling constant g^2 multiplied by a factor due to the density of states. In the case of state S1 with real part of the energy near E_d, this state actually follows Fermi's golden rule in three portions of the decay spectrum [the three portions laying between and well separated from the four band edges (see Fig. 10)].

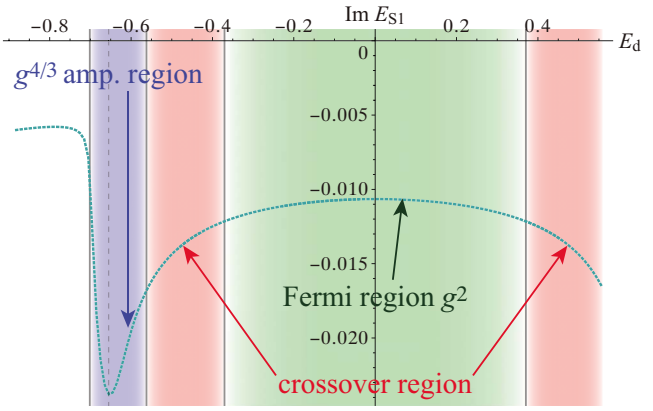

FIG. 22. (Color online) Here we show a magnified view (in comparison to Fig. 10) of the imaginary part of the energy (decay rate) for the solution S1 as a function of E_d for the domain between the two inner band edges. We have divided this domain into three types of regions: the Fermi region where Fermi's golden rule holds; the crossover region where this law begins to break down; and then the $g^{4/3}$ amplification region very near one of the singularities at the band edges (in this case, the lower inner band edge $-t_h + t_h'$ at the gray line). In this last region, Fermi's golden rule fails entirely.

We can easily obtain an approximate description of the decay rate in, for example, the innermost region between the two inner band edges $|E_d| \ll |t_h - t_h'|$ by applying the zeroth-order approximation $E_{S1} \approx E_d$ to the discrete dispersion equation [Eq. (11)]. Doing so, we obtain the first-order expression in the Fermi region as

$$E_{S1} = E_d - i\frac{g^2}{2}\left[\frac{1}{\sqrt{t_h^2 - (E_d + t_h')^2}} + \frac{1}{\sqrt{t_h^2 - (E_d - t_h')^2}}\right] + O(g^4)$$

$$(|E_d| \ll |t_h - t_h'|), \tag{69}$$

where the g^4 term gives the energy shift. Notice the factor that occurs in this expression from the density of states in Eq. (8) for both channels, just as Fermi's golden rule predicts. Of course, the divergence in these factors near the singularities is precisely the reason Fermi's golden rule breaks down in these cases. See Fig. 22 for a depiction of the three different types of regions for state S1, focusing in on the portion of the spectrum between the two inner band edges.

In order to obtain an understanding of how the decay rate varies in the crossover region, let us again reparametrize the

impurity energy E_d in terms of proximity to the lower inner band edge at $-t_h+t_h'$ according to $E_d \equiv (-t_h+t_h')+E_\lambda g^\lambda$ exactly as we did in Eq. (51) for the emerging QBIC. We are inside the amplification region for $\lambda \geq 4/3$, while $\lambda=0$ places us in the Fermi region. Hence, we are specifically interested in the region $0<\lambda<4/3$ that gives the crossover region.

However, while we have used the same reparametrization as in the previous calculation, in the present case it is convenient to introduce a slight variation in the usual expansion scheme. In this case, we will explicitly write our expansion in terms of real and imaginary contributions to the eigenenergy for S1 according to

$$E_{S1} \approx (-t_h+t_h')+E_\lambda g^\lambda + \Delta E_a g^a + \Delta E_b g^b + \ldots + i\Gamma_\alpha g^\alpha + i\Gamma_\beta g^\beta + \ldots \tag{70}$$

with each order ΔE_x contributing to the energy shift (the real part) and each $i\Gamma_x$ contributing to the decay rate (the imaginary part). In previous cases, such as the calculation for the emerging QBIC in Sec. III C 6, it has not been possible to explicitly separate these contributions in this way. This is because either the contributions have been mixed at a single order (a single term having both real and imaginary parts, such as occurred in Sec. IV A 1) or there have been complicated equalities that involve three or more terms (such as the case of the emerging QBIC expansion). In the present case, we find by inspection that the expansion breaks down along the lines of real and imaginary terms when we plug Eq. (70) into the dispersion equation [Eq. (11)]. Hence this expansion will ultimately aid us in sorting out the contributions at various orders.

By inspection we will find that the order $\alpha<a$ throughout the crossover region, such that the lowest-order contribution to the decay rate always dominates over that for the energy shift for S1. Further, we will find that $\lambda<\alpha$ for all values of λ in the crossover region. Precisely the opposite condition was true in the case of the emerging QBIC calculation in Sec. III C 6. This is one of the two key differences in the present case from the emerging QBIC case. The other difference is that the lowest-order value for the energy of the emerging QBIC was $-t_h+t_h'$, while in the case of the partially amplified state S1 the lowest order is $(-t_h+t_h')+E_\lambda=E_d$.

With the above considerations in mind, we plug our expansion (70) into the dispersion equation [Eq. (11)] to obtain

$$\begin{aligned}\Delta E_a g^a + \Delta E_b g^b + i\Gamma_\alpha g^\alpha + i\Gamma_\beta g^\beta \\ \approx \left(\frac{g^{2-\lambda/2}}{2\sqrt{-2t_h E_\lambda}} - \frac{i\Gamma_\alpha g^{\alpha-\lambda+(2-\lambda/2)}}{4\sqrt{-2t_h E_\lambda^3}} + \frac{E_\lambda g^{2+\lambda/2}}{8t_h\sqrt{-2t_h E_\lambda}} \right. \\ \left. - \frac{i\Gamma_\beta g^{\beta-\lambda+(2-\lambda/2)}}{4\sqrt{-2t_h E_\lambda^3}} + \cdots \right) + \left(\frac{g^2}{4\sqrt{-t_h'(t_h-t_h')}} \right. \\ \left. + \frac{(-t_h+2t_h')E_\lambda g^{2+\lambda}}{16t_h'\sqrt{-t_h'(t_h-t_h')^3}} + \cdots \right)\end{aligned} \tag{71}$$

after cancellation between the zeroth-order terms E_d that appear on both sides of the expansion. In previous cases we were often compelled to equate multiple terms on the RHS (possibly combined with a term on the LHS) of this type of expansion to obtain the order exponents and their respective coefficients. In the case of the above expansion we can actually equate a single term on the RHS with a single term on the LHS to obtain each of the order exponents, at least up to the first few terms that we have included.

We immediately recognize the lowest-order term on the RHS of Eq. (71) as the first term in the first set of parentheses since $2-\lambda/2<2$ for all $0<\lambda<4/3$. Noting the negative under the root, this term is purely imaginary. Thus we are immediately led to

$$\alpha = 2 - \frac{\lambda}{2}, \tag{72}$$

$$i\Gamma_\alpha = \frac{1}{2}\sqrt{-2t_h E_\lambda} = -\frac{i}{2}\sqrt{2t_h E_\lambda}, \tag{73}$$

which gives $\Gamma_\alpha = -\sqrt{2t_h E_\lambda}/2$. Here we have chosen the negative root for the decaying solution S1. Now let us examine the second term in the first set of parentheses on the RHS. Notice that while there is a negative under the root in this term, there is also a factor of $i\Gamma_\alpha$. Hence this term is real and must be set equal to one of the energy shift terms of the LHS; this will actually be the lowest-order term for the energy shift. A similar analysis can be used for each term that appears on the RHS of Eq. (71). Notice that every term on the RHS contains an imaginary factor due to a negative under the root in each denominator. Hence, all these terms will be pure imaginary except for those that contain a factor $i\Gamma_X$ for some order X. Hence we see that the second term in the first set of parentheses (order $g^{\alpha-\lambda+(2-\lambda/2)}$) determines the first-order correction for the energy shift, while the fourth term in the first set of parentheses (order $g^{\beta-\lambda+(2-\lambda/2)}$) gives the next order correction to this quantity,

$$a = \alpha - \lambda + \left(2 - \frac{\lambda}{2}\right), \tag{74}$$

$$b = \beta - \lambda + \left(2 - \frac{\lambda}{2}\right). \tag{75}$$

All other terms appearing on the RHS of Eq. (71) are imaginary.

Our task now reduces to determining which contributions dominate for a given value of λ in our range of interest, $0<\lambda<4/3$. The lowest-order correction for the energy shift is given, as we stated above, from the second term in the first set of parentheses on the RHS. Since we have already determined α, we can immediately obtain the order as $a=\alpha-\lambda+(2-\lambda/2)=4-2\lambda$. Then we also have $\Delta E_a = -i\Gamma_\alpha/(4\sqrt{-2t_h E_\lambda^3}) = 1/(16t_h E_\lambda^2)$. Finally, we will just find the order for the second-lowest-order contributions as our correction terms. It is easy to see that the next lowest-order correction for the decay rate (order β) comes from the first term in the second set of parentheses on the RHS; every other term on the RHS is already accounted for or has an order greater than 2. Hence we have $\beta=2$. Having obtained β, we can obtain the next correction for the energy shift as $b=\beta-\lambda+(2-\lambda/2)=4-3\lambda/2$.

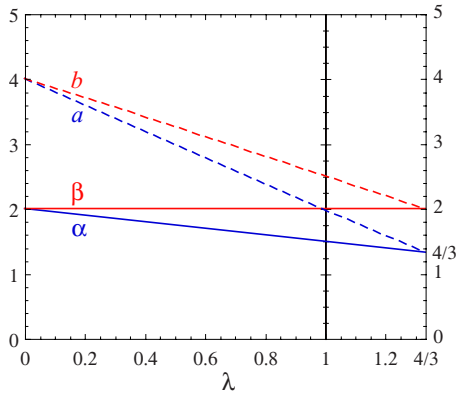

FIG. 23. (Color online) The dependence of the exponents α, β, a, and b in expansion (70) on the exponent λ in Eq. (51), as determined in the final expansion [Eq. (76)]. The solid lines indicate that the exponents affect the decay rate (the imaginary part of the eigenvalue), while the broken lines indicate that the exponents affect the energy shift (the real part).

Putting all this together, we can now write our original expansion (70) for the partially amplified decaying state S1 in the crossover region as

$$E_{S1} = E_d + \frac{1}{16 t_h E_\lambda^2} g^{4-2\lambda} + O(g^{4-3\lambda/2}) - i\left(\frac{1}{2\sqrt{2 t_h E_\lambda}} g^{2-\lambda/2} + O(g^2)\right) \quad (0 < \lambda < 4/3) \tag{76}$$

(see Fig. 23). We emphasize here that the first correction term, of order $4-3\lambda/2$, is the correction term for the energy shift, while the second correction term of order 2 is the correction to the decay rate up to our level of approximation. Hence we see that the decay rate in the crossover region follows the order $g^{2-\lambda/2}$ as λ varies from zero to 4/3. Note also that if we choose $\lambda=0$ we recover the correct order of g^2 for the Fermi region and if we choose $\lambda=4/3$ we recover the correct order in the amplification region of $g^{4/3}$, hence this result is certainly sensible. We will see in Sec. V B 3 that the factor $g^{-\lambda/2}$, which results from the singularity, also arises in relation to the QBIC effect when the hopping parameter t_h' approaches the value of t_h.

B. Local density of states and the Fano effect

In a nonhomogenous system, it is known that the states available to the electron are not spatially uniform but instead may be clumped together in some places more than others. Hence, for such systems it is useful to introduce the local density of states (LDOS) $\rho_r(E)$ as a way of measuring the number of states (as a function of E) at a certain location r in the system. In our case, our primary interest is the impurity site that breaks the homogeneity of the two-channel system. We will therefore focus on the LDOS at this site in the present section. The LDOS function at a certain point in space is defined to be proportional to the imaginary part of the Green's function at that point divided by a factor of π.[30]

The LDOS is a convenient quantity for connecting with experiment as it can be probed directly through scanning tunneling spectroscopy using scanning tunneling microscopy (STM) probe. The STM is a powerful tool, useful in the determination of the structural and electronic properties of surfaces on the atomic scale.[40] The STM probe itself is essentially a small metal electrode with a very narrow tip (tip radius of ~100 Å). When the tip of the probe is brought very close (~10 Å) to the sample surface, electrons may tunnel through the vacuum barrier separating the tip and the sample. This tunneling current I_T is sensitive to the distance and the bias voltage V_B between the tip and the sample. Varying V_B effectively shifts the Fermi energy in the probe; this changes the range of energies in which electrons are allowed to participate in the tunneling. By studying how I_T changes with V_B, the experimentalist may probe the LDOS at a particular point on the sample surface (e.g., at the adatom). Using first-order perturbation theory, it can be shown that the quantity $d \ln I_T / d \ln V_B$ is proportional to the LDOS measured at the effective Fermi level in the probe. This particular application of the STM probe is referred to as scanning tunneling spectroscopy. While this technique may not work in such a straight-forward manner for Fermi energies near the band edges, there are methods for dealing with this case as well.[41]

Below we will present the LDOS function at the adatom site for various values of the adatom impurity energy E_d. When we choose a value for E_d near one of the inner band edges, we will find an example of the asymmetric Fano effect due to interference between multiple resonant states that have nearly the same real part of the eigenvalue but differing decay rates. As a special case, we will also present the LDOS for the case in which E_d lies inside the crossover region. In fact we will focus on the $\lambda=1$ case discussed in Sec. III C 6 for the emerging QBIC such that the spectral weight of this state is amplified relative to the ordinary QBIC. We will see that the peak associated with the emerging QBIC in the LDOS spectrum will also have the characteristics of the Fano interference. This results in the peak being a more prominent feature in the spectrum than in the case of the ordinary QBIC.

Since we have already defined the Green's function for the impurity site in Eq. (9), we can immediately write the LDOS function $\rho_d(E)$ (Ref. 30) as

$$\rho_d(E) \equiv \pm \frac{\mathrm{Im}\, G_{dd}(E)}{\pi}. \tag{77}$$

Ordinarily the LDOS is simply defined with a negative sign; however, since we are dealing with a more complex Green's function in a four-sheeted Riemann surface, we find that it is necessary to use the positive sign in the case $E_d<0$ to maintain physically sensible results. We plot this function for four representative cases in Figs. 24(a)–24(d).

In Fig. 24(a) we have plotted $\rho_d(E)$ for the same values, including $E_d=0.3$, as we used in Table I in Sec. III A. Note that we have labeled the real parts of the eigenvalues for each pole of the Green's function; we have used a blue dot to label the two poles S1 and RQ4 that lie near to E_d (the real

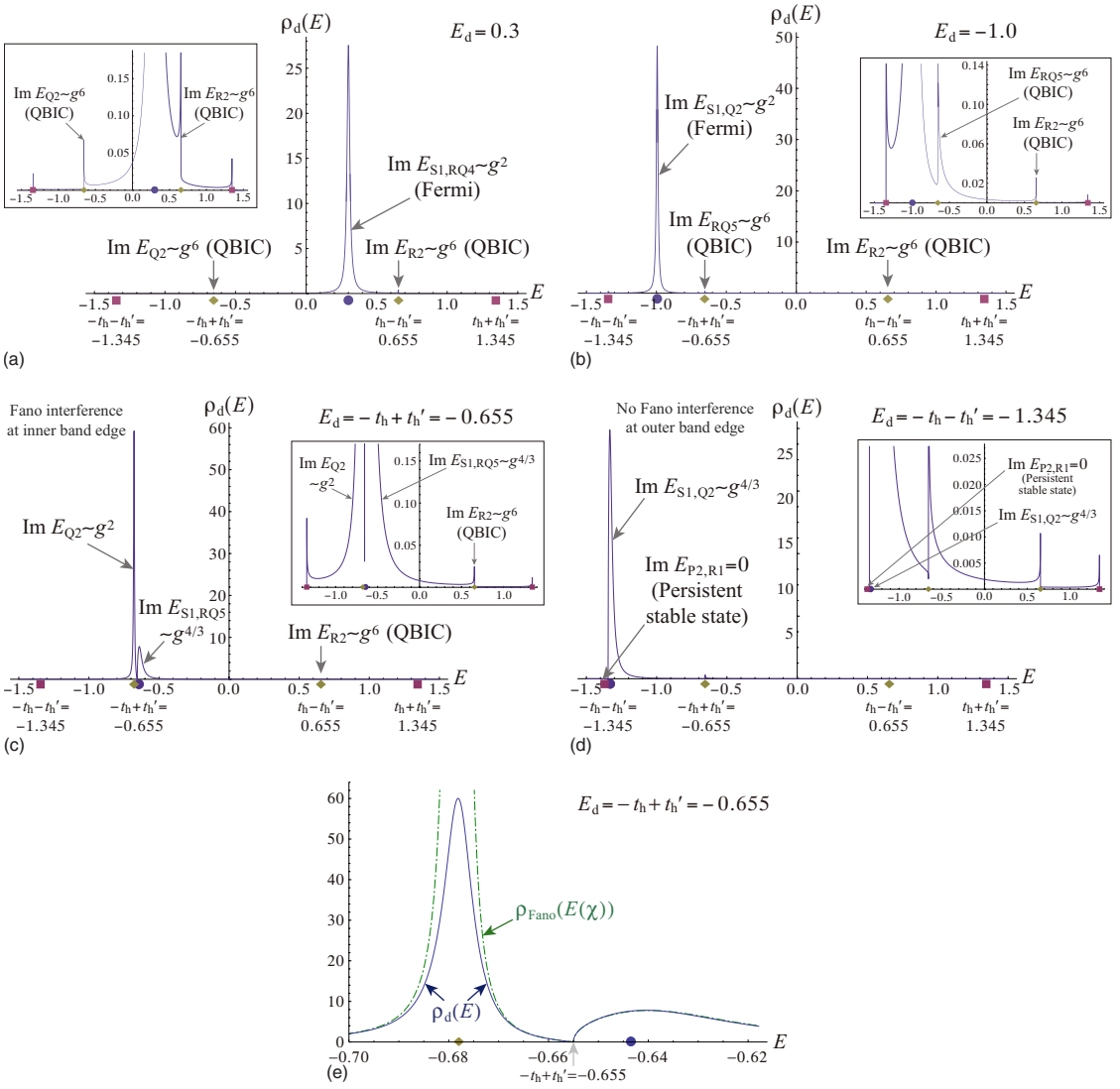

FIG. 24. (Color online) The LDOS function $\rho_d(E)$ for four representative cases: in (a) we plot the case $E_d=0.3$, which is the same value as presented in Table I; in (b) we plot the case $E_d=-1.0$, which is the same value as presented in Table II; in (c) we plot the case $E_d=-t_h+t_h'=-0.655$, in which we see the Fano effect due to interference between multiple poles near the inner band edge; and in (d) we plot the case $E_d=-t_h-t_h'=-1.345$. In each case we use the typical values $t_h=1$, $t_h'=0.345$, and $g=0.1$. The main plot in each case shows the full scale of the vertical axis over the entire domain of the two energy spectra, while the inset magnifies near the origin for the vertical axis while also presenting the entire energy domain. The blue dot shows the real part of the energy eigenvalue for either Fermi-like states or states with amplified decay rate. Meanwhile the gold diamonds label either QBIC or emerging QBIC states that lie on the inner band edges and the purple squares show the persistent stable states that always lie just outside the outer band edges. (e) A closer view of the LDOS function $\rho_d(E)$ (solid blue curve) near the inner band edge $-t_h+t_h'$ for the value $E_d=-t_h+t_h'=-0.655$ used in the panel (c). We also plot the approximate form for the Fano profile $\rho_{Fano}[E(\chi)]$ (chained green curve) given in Eq. (82). The horizontal axis is the ordinary energy scale E [or $E(\chi)$ for the chained green curve] magnified near the lower inner band edge. The blue dot denotes the location of the real parts of the poles S1 and RQ5 with decay rate $\sim g^{4/3}$, while the gold diamond gives the location of the real part of the pole Q2 associated with the band edge and having a smaller decay rate $\sim g^2$.

part of these two poles lie almost directly on top of one another and are indistinguishable in this graph). In this case, S1 and RQ4 follow the Fermi decay behavior. We then use golden diamonds to label the real parts of the QBIC states Q2 and R2 at the two inner band edges. Finally we use purple squares to label the persistent stable states at the outer band edges. These latter states are of course purely real. It is clear from the plot that the Fermi-like resonance states S1 and RQ5 dominate the spectrum over the poles that lie on the inner and outer band edges. This is consistent with our expectations in the case of the full QBIC since we have shown in Sec. III C 5 that the residue for the QBIC states is much smaller than the Fermi-like states.

Next, in Fig. 24(b) we have plotted $\rho_d(E)$ for the value $E_d=-1.0$ that we used in Table II. Again we see that the Fermi states lying near the impurity energy E_d dominate over the QBIC states at the band edges.

In Fig. 24(c) we plot $\rho_d(E)$ for the case where the impurity energy lies directly on the lower inner band edge $E_d=-t_h+t_h'$, which is precisely the case ($g^{4/3}$ amplification re-

gion) for which we have obtained the analytic expansions for states S1, RQ5, and Q2 given in Eqs. (67) and (68). We remind the reader that when the impurity energy lies near to (or at) this band edge, state Q2 (golden diamond here) does not obey the QBIC behavior here but instead has a decay rate of the order g^2. Meanwhile states S1 and RQ5 (blue circle) have decay rates of order $g^{4/3}$ due to the band-edge divergence.

Investigating Fig. 24(c) we see that a unique phenomenon has emerged in the LDOS profile in this case: two peaks appear together here around the band edge $-t_h+t_h'$ with an asymmetric overall shape. Indeed this asymmetric shape is a result of interference between the two discrete poles with a very large decay rate (S1 and RQ5 with decay rate $\sim g^{4/3}$) and the pole with a smaller decay rate (Q2 with decay rate $\sim g^2$). This precise effect was previously explained for the case of only one pole with large decay rate and one pole with a smaller decay rate,[28,29] although note that in the present case the taller peak in Fig. 24(c) is associated with the state with the smaller decay rate. Also note that this asymmetric Fano effect occurs over a wide range of values near the inner band edges. We focus for now on the special case $E_d=-t_h+t_h'$ because it is straightforward in this case to obtain some approximations that give insight into the phenomenon as a whole. We return to this point momentarily.

Beforehand, consider Fig. 24(d) in which we plot the LDOS function for the case where the impurity energy this time lies directly on the outer band edge $E_d=-t_h-t_h'$. In this case, no Fano effect occurs because there are only two resonant states present (S1 and Q2, blue circle) and they both have decay rates of the same order $\sim g^{4/3}$ that are almost equal. There are also two persistent stable states present (P2 and R1, purple square) near the outer band edge, but they are both purely real and hence in this case there is no interference effect.

Returning to the case of Fig. 24(c) with E_d at the lower inner band edge, in Fig. 24(e) we plot a magnified view of $\rho_d(E)$ (solid blue curve) near the inner band edge $-t_h+t_h'$, where the Fano effect occurs. The antisymmetric shape is quite clear here. By using a slight variation in our standard perturbation method in this paper, we can obtain a useful approximation for analytically describing the shape of the asymmetric Fano peak. In order to obtain this expression, we set $E_d=-t_h+t_h'$ in $\rho_d(E)$ and then reparametrize the energy variable E according to

$$E(\chi) \equiv -t_h + t_h' + \chi g^{4/3}. \tag{78}$$

We choose this particular form as a simple ansatz reflecting the fact that the $g^{4/3}$ behavior is the dominant characteristic in this region. Our choice is borne out by the accuracy of the resulting approximation. Plugging our reparametrization into $G_{dd}(E)$ and expanding, we obtain

$$G_{dd}(E(\chi)) = \left(\chi g^{4/3} + \frac{g^2}{2} \left\{ \frac{1}{\sqrt{(-t_h+2t_h')^2 - t_h^2 + 2[(-t_h+2t_h')]\chi g^{4/3} + \cdots}} + \frac{1}{\sqrt{-2t_h\chi g^{4/3} + \chi^2 g^{8/3} + \cdots}} \right\} \right)^{-1}. \tag{79}$$

We reorganize and expand the roots in the denominator on the RHS to obtain

$$G_{dd}(E(\chi)) \approx \left\{ \chi g^{4/3} + \frac{g^{4/3}}{2\sqrt{-2t_h\chi}} \left(1 + \frac{\chi}{4t_h} g^{4/3} + \cdots \right) + \frac{g^2}{4\sqrt{-t_h'(t_h-t_h')}} \left[1 + \frac{(-t_h+2t_h')}{4t_h'(t_h-t_h')} + \cdots \right] \right\}^{-1}. \tag{80}$$

Finally we expand the denominator itself and find

$$G_{dd}(E(\chi)) \approx \frac{g^{-4/3}}{(\chi + 1/2\sqrt{-2t_h\chi})} \left\{ 1 - \frac{1}{4\sqrt{-t_h'(t_h-t_h')}[\chi + 1/2\sqrt{-2t_h\chi}]^2} g^{-2/3} + O(g^{4/3}) \right\}. \tag{81}$$

Notice that the denominator of the coefficient in this expression will be complex for values of $\chi>0$. According to our reparametrization [Eq. (78)] this is equivalent to an energy value $E>-t_h+t_h'$, lying to the right of the lower inner band edge. Since $\rho_d(E)$ is proportional to Im $G_{dd}(E)$, this means that the first term (order $g^{-4/3}$) will give the lowest-order contribution to the LDOS profile for $\chi>0$. On the other hand, for values of $\chi<0$, such that E lies to the left of the lower inner band edge, the first term on the RHS of Eq. (81) will be purely real. However, notice that the second term contains an explicit factor of i due to the negative under the root in the denominator. Hence this term is complex on *both* sides of the band edge, $\chi<0$ and $\chi>0$. Factoring out this term i, we can then take the real part of this term to find its contribution to the LDOS profile. We can therefore write our approximate LDOS Fano function $\rho_{Fano}[E(\chi)]$ as follows:

$$\rho_{\mathrm{Fano}}(E(\chi)) = \begin{cases} \mathrm{Re}\left[\dfrac{1}{4\pi\sqrt{t_h'(t_h - t_h')}(\chi + 1/2\sqrt{-2t_h\chi})^2}\right] g^{-2/3} + O(g^{2/3}) & (\chi < 0) \\ \mathrm{Im}\left[\dfrac{1}{\pi(\chi + 1/2\sqrt{-2t_h\chi})}\right] g^{-4/3} + \mathrm{Re}\left[\dfrac{1}{4\pi\sqrt{t_h'(t_h - t_h')}(\chi + 1/2\sqrt{-2t_h\chi})^2}\right] g^{-2/3} + O(g^0 \sim 1) & (\chi > 0) \end{cases} . \tag{82}$$

Notice that the factor in the denominator $(\chi + 1/2\sqrt{-2t_h\chi}) = 0$ at the value $\chi = -1/2t_h^{1/3}$ for $\chi < 0$. Hence there is a divergence that appears in the first line of Eq. (82) only. Plugging this value of χ into our reparametrization [Eq. (78)], we see that his value is equivalent to $E = (-t_h + t_h') - g^{4/3}/2t_h^{1/3}$. This is precisely the first-order approximation for the position of the pole Q2 given in Eq. (68). Hence, this divergence represents the presence of the pole with the smaller decay rate ($\sim g^2$) to the left of the lower inner band edge [gold diamond in Fig. 24(e)]. We can clearly see this divergence in the chained green curve in Fig. 24(e), which represents our approximation for the Fano effect $\rho_{\mathrm{Fano}}[E(\chi)]$. Our approximation function captures both the qualitative and quantitative characteristics of the asymmetric Fano behavior, including the fact that $\rho_{\mathrm{Fano}}[E(\chi)] = 0$ right at the inner band edge ($\chi = 0$) and the wide shallow peak around the states S1 and RQ5 (blue dot) with the larger (greater width) decay rates $\sim g^{4/3}$. In fact, apart from the divergence the two graphs are almost indistinguishable.

Finally we consider the LDOS function for another situation in Fig. 25. Here we plot $\rho_d(E)$ for the case $E_d = -0.6$ ($\lambda = 1$), which places the system exactly at the point in the crossover region that we have discussed previously in Sec. III C 6. Hence, the decay rates for S1 and RQ5 (blue dot) are partially amplified by the singularity at $-t_h + t_h'$ with decay rate $\sim g^{3/2}$ as described by Eq. (76), while state Q2 (gold diamond) is an emerging QBIC state with small decay rate $\sim g^3$ as described in Sec. III C 6. As can be seen in the graph, the Fano effect is still present due to the proximity of the two states with larger decay rates and the emerging QBIC state, though the effect is less pronounced now. The emerging QBIC state Q2 is clearly represented by the thin peak owing to the very small decay rate, as we have seen near the band edges in the previous plots. In this case, however, this peak is a prominent feature of the LDOS spectrum. Indeed, the Q2 peak here is comparable to the other primary feature in the spectrum, the S1/RQ5 peak resonant with the impurity energy E_d. As we have seen in Figs. 24(a) and 24(b), the peak resonant with E_d in the most typical cases completely dominates the LDOS spectrum. In this case, the emerging QBIC with enhanced spectral weight also makes a strong presence. Judging from the asymmetric line shape in Fig. 25, this strong presence seems to be attributable, at least in part, to the Fano interference.

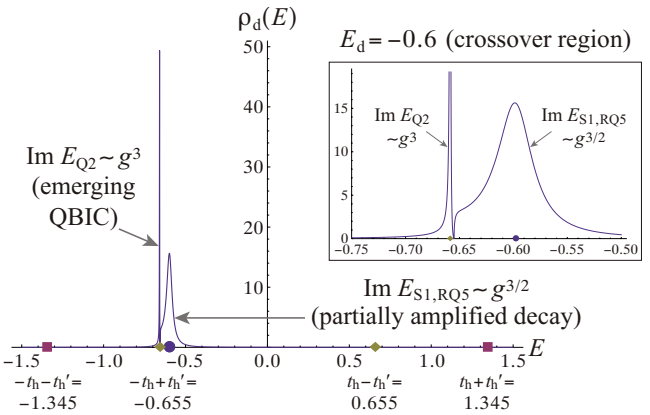

FIG. 25. (Color online) The LDOS function $\rho_d(E)$ for the case $E_d = -0.6$, which places the system inside the crossover region described in Sec. III C 6. The decay rates for the states S1 and RQ5 (blue dot) are therefore partially amplified by the nearby singularity at the inner band edge $-t_h + t_h'$ and the asymmetric Fano line shape is still present. Meanwhile, the emerging QBIC state Q2 (gold diamond near $-t_h + t_h' = -0.655$) is clearly visible in the spectrum with a tall thin peak. We use the typical numbers $t_h = 1$, $t_h' = 0.345$, and $g = 0.1$. Inset: a magnified view near the inner band edge.

V. ENERGY SPECTRUM ANALYSIS IN TWO SPECIAL CASES

In this section, we will briefly consider the energy spectrum analysis for two special cases. In the first special case ($t_h' = 0$) the two-channel model reduces to the single-channel model when the chain-to-chain hopping parameter t_h' vanishes. Even though this case might seem trivial at first glance, it is instructive to see the relation of the two-channel model to the single-channel model. Then we will consider the case $t_h' = t_h$. Here we will find that the 12th-order dispersion polynomial reduces to a tenth-order polynomial, while the QBIC decay rate is amplified such that it is proportional to g^4 in the first-order perturbation; both embedded singularities play a role in this modified QBIC effect as we will show.

A. Energy spectrum for $t_h' = 0$ case

Here we will comment on the case $t_h' = 0$, in which the chain-to-chain hopping parameter vanishes. Since the adatom is then coupled to only one chain, it is to be expected that this system should reduce to the single-chain model (along with an additional uncoupled chain). Indeed, considering the discrete dispersion equation [Eq. (11)] we see that for $t_h' = 0$ the two terms on the RHS containing the square roots will agree. Therefore, in the case where the sign of the two square roots agrees, these two terms will combine to

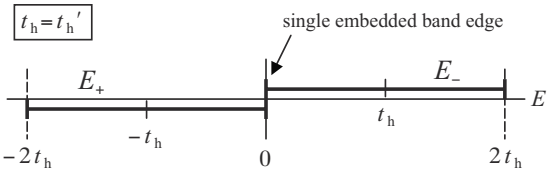

FIG. 26. Band structure for the $t_h'=t_h$ case with a single "unified" embedded band edge in the center of the spectrum.

give a new dispersion equation equivalent to that for the single-channel model [equal to Eq. (26) after setting $t_h'=0$ and replacing with the renormalized coupling constant $g' \to \sqrt{2}g$]. This case corresponds to sheets I and IV in the complex energy surface, which contain four solutions (two in each sheet). These four solutions then behave precisely as the four solutions to the quartic dispersion polynomial in the original single-channel model.

Meanwhile, for the case in which the signs of the two square roots in Eq. (11) are opposite, then these two terms cancel and the dispersion equation becomes trivial. This case corresponds to sheets II and III, which contain eight solutions. Meanwhile, since the two branch cuts in this case overlap exactly, sheets II and III become mathematically (and physically) inaccessible. If one travels through the branch cut in sheet I, one will always appear in sheet IV (and vice versa). Hence the energy surface is effectively two sheeted and, for our purposes here, essentially equivalent to that in the single-chain system.

B. Energy spectrum for $t_h'=t_h$ case

In the case $t_h'=t_h$, the two inner band edges will overlap to form a single embedded band edge as indicated in Fig. 26. Note that, in a certain sense, both band edges are still present. In fact, we will find that in this case the van Hove singularity from one overlapping band edge will actually amplify the QBIC decay rate that results from the van Hove singularity of the other band edge, so that the decay rate will now be proportional to g^4. This is a unique combination of two previous effects, both resulting from the van Hove singularity.

1. Tenth-order dispersion polynomial for the $t_h'=t_h$ case

If we set $t_h'=t_h$ in Eq. (11), then the dispersion equation for the adatom becomes

$$z - E_d - \frac{g^2}{2\sqrt{|z|}}\left[\frac{1}{\sqrt{z+2t_h}} + \frac{1}{\sqrt{z-2t_h}}\right] = 0. \tag{83}$$

Note that here the position of a solution in the complex energy surface should be determined only by the two square roots $1/\sqrt{z \pm 2t_h}$; the overall factor of $1/\sqrt{|z|}$ plays no role in this determination. However, this overall factor represents the presence of a van Hove singularity at $z=0$ in both bands.

As before, we can square this equation twice to find an equivalent tenth-order dispersion polynomial; hence two solutions have vanished from the system in comparison to the general case. Specifically, the two solutions RQ4 and RQ5 are no longer present. Note that the QBIC solutions Q2 and R2 remain in this simplified system.

As was done in Sec. III A and in Fig. 6, it is more convenient for the purpose of placement of each solution in the correct Riemann sheet to solve

$$-t_h \cos K_+ - t_h = -t_h \cos K_- + t_h = E_d + g^2\left(\frac{1}{2it_h \sin K_+} + \frac{1}{2it_h \sin K_-}\right) \tag{84}$$

with respect to $K_\pm$ than to solve the discrete dispersion equation [Eq. (83)] with respect to $z=E$. The imaginary parts of the solutions of the above simultaneous equations give the correct Riemann sheet. The eigenenergy of each solution is then given by the channel dispersion equations, $E=-t_h \cos K_\pm \mp t_h$.

The dependence of the real and imaginary parts of all the solutions on E_d can be seen in Figs. 27 and 28, respectively, for the value $g=0.1$ for the coupling.

2. Modified QBIC effect

As in the general case, solutions Q2 (for $E_d \gg 0$) and R2 (for $E_d \ll 0$) are QBIC states. Their real parts behave similar to the persistent stable states in that they lie near to the embedded band edge at $z=0$ in Fig. 27. However, they have a small nonzero decay rate as can be seen in Fig. 28. We can obtain an approximate form for the energy eigenvalue for these states in a manner similar to that we employed before in the general case. Figure 27(b) shows that the real part of the energy for Q2 is also small with a value that lies near the origin on the y axis. Hence, we assume that the expansion of E_{Q2} begins with the order g^α with $\alpha>0$ as $E_{Q2}=\chi_\alpha g^\alpha + \cdots$. Applying this expansion in Eq. (83) and using a similar argument as that given in Sec. III B give

$$\sqrt{\chi_\alpha} = g^{2-\alpha/2}\frac{1}{2\sqrt{2t_h E_d}}(1-i), \tag{85}$$

in which the two terms in parentheses (both of which are necessary for E_{Q2} to be complex) have been contributed, respectively, by the two bracketed terms on the LHS of Eq. (83) and the factor $1/\sqrt{|z|}$ associated with the van Hove singularity in *both* terms has resulted in the factor $g^{2-\alpha/2}$. We then obtain the condition for the order of α as $\alpha=4$ as well as $\chi_\alpha=-i/(4t_h E_d^2)$, from which we can write

$$E_{Q2} = -i\frac{g^4}{4t_h E_d^2} + O(g^8). \tag{86}$$

We see that state Q2 is still quasistable in comparison to the ordinary decay rate proportional to g^2. However, the QBIC decay rate has been amplified, so that it is proportional to g^4 [instead of g^6 in the general case as given in Eq. (41)] due to the overlapping band edges. In a sense, the embedded van Hove singularity at $z=0$ from the E_- band has resulted in a QBIC state, while the singularity from the E_+ band has amplified the usual decay rate of g^6 to g^4. Solution R2 has the same behavior for $E_d \ll 0$ with the role of the bands reversed.

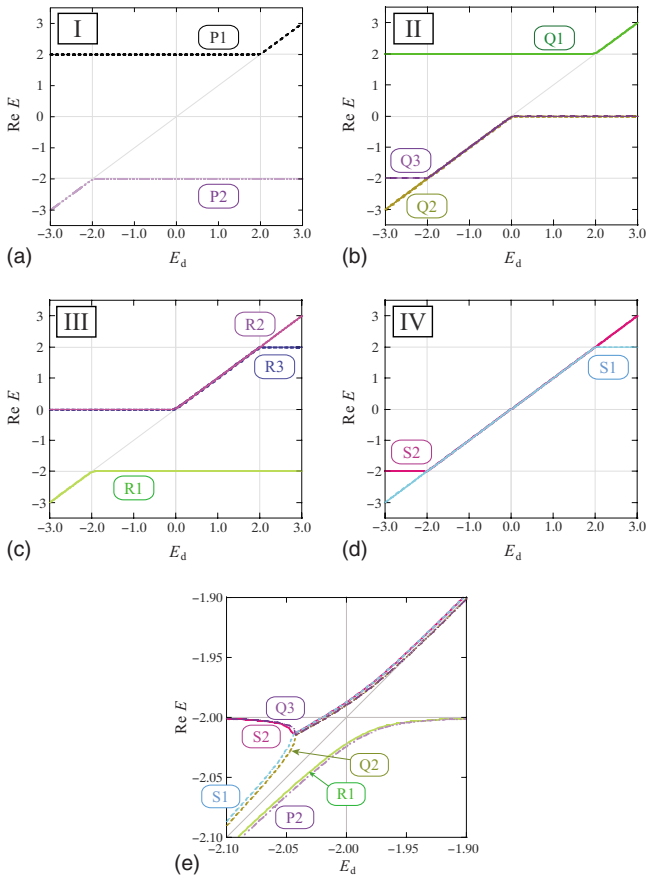

FIG. 27. (Color online) Real part of the energy for the ten solutions of the simplified dispersion equation [Eq. (83)] as a function of E_d for the special case $t_h'=t_h$ with the choice $g=0.1$. The unit of the energy is $t_h=1$. In the top, (a)–(d), each solution is plotted in the corresponding Riemann sheet. The overlapping curves represent a complex conjugate pair, for which the real part of the energy is exactly the same. The vertical and horizontal gray lines represent the three van Hove singularities. In the bottom (e), the lower left-hand corners at the top (a)–(d) are shown with all Riemann sheets superimposed.

Indeed, the channel weight function [Eq. (43)] reduces to

$$\theta(E) = \sqrt{\frac{E+2t_h}{E-2t_h}} \tag{87}$$

for $t_h'=t_h$ and gives $\theta(E_{Q2}) \sim i$ for the specific case of the QBIC state. Thus both channels contribute equally in this modified QBIC effect.

3. QBIC effect in transition to the modified g^4 case

In Secs. III C 6 and IV A 2, we studied the behavior of the emerging QBIC and the (partial) decay rate amplification in the crossover region, respectively. Here we consider a similar type of crossover behavior, though in this case we will vary the value of t_h' instead of E_d. In particular, we will now investigate the details of how the QBIC decay rate transitions between the g^4 behavior for the special case $t_h'=t_h$ and the generic case of the g^6 behavior for t_h' well separated from t_h (more specifically, $t_h' \ll t_h$). Following the spirit of our previous analysis, we reparametrize t_h' according to

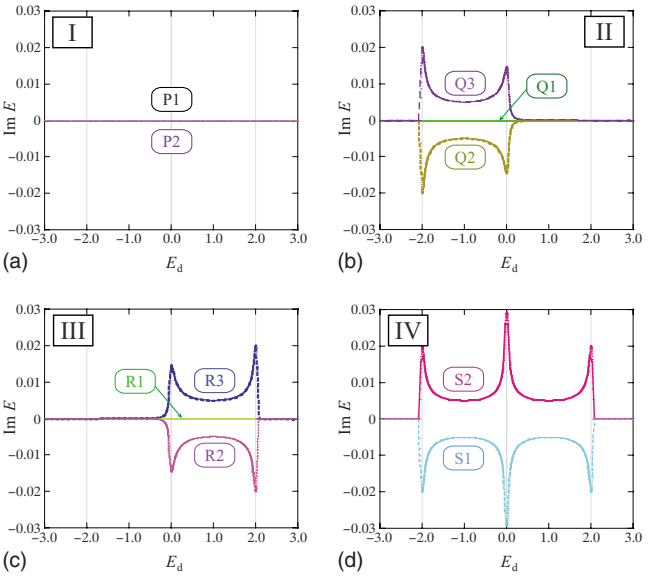

FIG. 28. (Color online) Imaginary part of the energy for the six complex solutions of the simplified dispersion equation [Eq. (83)] as a function of E_d for the special case $t_h'=t_h$ with the choice $g=0.1$. The unit of the energy is $t_h=1$. The vertical gray lines represent the three van Hove singularities.

$$t_h' = t_h - \tau g^\lambda. \tag{88}$$

Similar to the previous crossover analyses, we will find that the g^4 behavior for the QBIC decay rate appears precisely in the region where $\lambda=4$. Hence our range of interest will be $\lambda=0$ (the generic g^6 case) up to $\lambda=4$.

Applying this reparametrization to the discrete dispersion equation [Eq. (11)] yields the result

$$E_{Q2} = -\tau g^\lambda - \frac{1}{8t_h E_d^2} g^4 + O(g^{4+\lambda}) - i\left(\frac{1}{16t_h E_d^3 \sqrt{t_h \tau}} g^{6-\lambda/2} + O(g^{6+\lambda/2}, g^{8-\lambda})\right). \tag{89}$$

(Equally well, we can just plug the reparametrization for t_h' into the generic approximation [Eq. (41)], which gives the above result immediately upon expansion.) This result is again consistent with our expectations since the decay rate for Q2 will vary from first-order g^6 dependence for $\lambda=0$ and g^4 dependence for $\lambda=4$. Note the presence of the familiar $g^{-\lambda/2}$ factor, which is the same factor that appears in Eq. (76) for the crossover to the $g^{4/3}$ amplification region in the case of state S1. The r-appearance of this factor seems to indicate that this is a generic "amplification" behavior resulting from the one-dimensional van Hove singularity. This view is supported by noting that this factor does not appear in Eq. (52), in which there is no decay rate amplification occurring; the destabilization that occurs in that case is a result of the embedding continuum and not of the embedded singularity.

VI. CONCLUDING REMARKS

We have demonstrated the existence of the QBIC state in the context of a two-channel quantum wire with an attached adatom impurity. Ordinarily, an electron in the impurity with an energy deep inside of the conduction band of the wire would be expected to decay and travel along the length of the wire. We might also expect that we could describe the decay rate using Fermi's golden rule. However, due to the combined effect of two overlapping conduction bands (with van Hove singularities at the band edges), we have shown that a QBIC electron will remain stable inside the impurity for ordinary time scales. In particular, we have demonstrated the connection between the QBIC state and the persistent stable state that results from the van Hove singularity at the band edge in the single-channel model. In the two-channel model, this persistent stable state is slightly destabilized as a result of being embedded in a second conduction band.

We have also shown in Eq. (41) that the characteristic decay rate for the QBIC is generally on the order of g^6, although this may be modified under certain conditions, such as the case $t_h'=t_h$ in the two-channel model (under which Im $E\sim g^4$). Then there are the crossover cases, such as the crossover from the g^6 decay rate to the g^4 value as t_h' approaches t_h, described in Eq. (89). Most importantly, there is the case of the emerging QBIC described in Sec. III C 6 that provides the most obvious starting place for experimental detection. In this case, the QBIC peak in the LDOS profile is amplified due to the Fano interference, as we have shown in Fig. 25.

While we have demonstrated the above behaviors specifically for the two-channel quantum wire, it is easy to show that the QBIC effect should occur in other one-dimensional multichannel models which have the characteristic square root divergence in the DOS given in Eq. (8). For instance, in a letter[5] by Petrosky *et al.*, the authors explored the effects of the divergent singularity in the photon density of states at the cutoff frequency in the interaction between an excited oscillator (diatomic molecule, for instance) and the lowest transverse electric (TE) mode in a rectangular waveguide. The QBIC effect will also occur in this waveguide system when the oscillator interacts with the second-lowest TE mode, which has a cutoff frequency embedded in the continuum of the lowest TE mode.

Hence, the origin of the QBIC effect is quite different than that of the BIC effect originally proposed by von Neumann and Wigner. On the one hand, we can associate each QBIC state with a divergent band-edge singularity embedded in the continuum of another energy band. On the other hand, the BIC states are associated with zeros in the interaction potential that occur in the continuous energy spectrum for certain models with an oscillating potential. Hence the QBIC is more closely associated with the DOS function, while the BIC is more closely associated with the interaction potential. It is also possible (even likely) that the QBIC effect will appear in some two-dimensional systems (such as a two-dimensional tight-binding lattice) that have a characteristic logarithmic divergence in the DOS[3,39] that may be embedded in the continuum even in a single-channel model.

As we remarked in our previous letter,[1] because our quasibound state has a small decay rate (imaginary component of the eigenenergy), it is not, strictly speaking, "in continuum." However, this decay rate is extremely small, such that the QBIC state should behave as if it was a bound state with real part of the eigenenergy deeply embedded in the continuum even on relatively large time scales. In this sense, the QBIC will essentially behave as the BIC under actual experimental conditions. Meanwhile, the BIC is a true bound state with a purely real energy spectrum but only under ideal conditions. Since the BIC exists only at discrete points (with zero measure) in the continuum any noise in the system (such as thermal noise) in an experiment may actually lead to a small decay rate for the BIC. On the contrary, since the QBIC exists over a wide range of the energy spectrum (with continuous measure), it is robust against noise. Hence, it may be easier to prepare the QBIC in experiment.

It should be mentioned that there may be certain models with embedded singularities in which the QBIC effect due to the DOS singularities will be washed out as a result of the form of the interaction potential. There exist some examples of a single-channel model in which the interaction potential washes out the divergent behavior of the singularity and prevents the persistent stable state from forming.[6,19,20]

ACKNOWLEDGMENTS

The authors thank Ingrid Rotter, Satoshi Tanaka, and E. C. G. Sudarshan for useful discussions. S.G. would like to thank the National Science Foundation and the Japan Society for the Promotion of Science for their support, as well as Satoshi Tanaka for his hospitality during a stay in Japan. This material is based on work supported by the National Science Foundation under Grant No. 0611506. The work was supported partly by the Murata Science Foundation as well as by the National Institutes of Natural Sciences undertaking Forming Bases for Interdisciplinary and International Research through Cooperation Across Fields of Study and Collaborative Research Program (Grant No. NIFS08KEIN0091) and Grants-in-Aid for Scientific Research (Grant No. 17340115, No. 17540384, and No. 20340101) from the Ministry of Education, Culture, Sports, Science and Technology. N.H. acknowledges support by Core Research for Evolutional Science and Technology (CREST) of Japan Science and Technology Agency.

APPENDIX: NUMERICAL METHOD FOR TIME EVOLUTION SIMULATION OF WAVE FUNCTIONS

In this appendix we describe our numerical method for obtaining the time evolution of the wave functions of the resonant states of the two-channel Hamiltonian. We rely on the method which was proposed in previous work[27] to solve the time-dependent Schrödinger equation accurately (despite truncation of the domain of x in numerical calculations). The time-dependent Schrödinger equation is given by

$$i\hbar\frac{\partial}{\partial t}|\Psi(t)\rangle = \hat{\mathcal{H}}|\Psi(t)\rangle, \tag{A1}$$

and the initial condition is fixed as

$$|\Psi(0)\rangle = |\psi\rangle, \tag{A2}$$

where $|\psi\rangle$ is the eigenstate of $\mathcal{H}$ in Eq. (12). We define the time-dependent wave function as follows:

$$\Psi_{\mathrm{d}}(t) \equiv \langle \mathrm{d}|\Psi(t)\rangle, \quad \Psi(x,y;t) \equiv \langle x,y|\Psi(t)\rangle, \tag{A3}$$

where $y=1,2$. The vector form of the wave functions is given by

$$\vec{\Psi}_y(x,t) \equiv \begin{pmatrix} \Psi(x,1;t) \\ \Psi(x,2;t) \end{pmatrix} = e^{-iEt}\vec{\psi}_y(x). \tag{A4}$$

We restrict the region $|x| \le L, (L \ge 1)$ to compute the time evolution of the wave function. The steady wave function $\vec{\psi}(x)$ in Eq. (17) has the following recursion property:

$$\begin{aligned} \vec{\psi}_y(L+1) &= U\vec{\psi}_\sigma(L+1) \\ &= U\left\{A_+ e^{iK_+(L+1)}\begin{pmatrix}1\\0\end{pmatrix} + A_- e^{iK_-(L+1)}\begin{pmatrix}0\\1\end{pmatrix}\right\} \\ &= U\begin{pmatrix} e^{iK_+} & 0 \\ 0 & e^{iK_-}\end{pmatrix}U^{-1}U\vec{\psi}_\sigma(L) \\ &= V_{\mathrm{eff}}\vec{\psi}_y(L), \end{aligned} \tag{A5}$$

where we have used Eqs. (14) and (17). We have defined the effective potential V_{eff} as

$$V_{\mathrm{eff}} \equiv U\begin{pmatrix} e^{iK_+} & 0 \\ 0 & e^{iK_-}\end{pmatrix}U^{-1} = \frac{1}{2}\begin{pmatrix} e^{iK_+}+e^{iK_-} & e^{iK_+}-e^{iK_-} \\ e^{iK_+}-e^{iK_-} & e^{iK_+}+e^{iK_-}\end{pmatrix}, \tag{A6}$$

which we have extended from the scalar form of the chain model.[2,27,28] At $x=\pm L(L>0)$, using the effective potential [Eq. (A6)], the left term of the time-dependent Schrödinger equation [Eq. (A1)] becomes

$$\begin{aligned} \hat{\mathcal{H}}_{\mathrm{eff}}\vec{\Psi}_y(\pm L,t) &= -\frac{t_{\mathrm{h}}}{2}\{\vec{\Psi}_y[\pm(L-1),t] + \vec{\Psi}_y[\pm(L+1),t]\} \\ &\quad - t'_{\mathrm{h}}\begin{pmatrix}0&1\\1&0\end{pmatrix}\vec{\Psi}_y(\pm L,t) \\ &= -\frac{t_{\mathrm{h}}}{2}\vec{\Psi}_y[\pm(L-1),t] - \frac{t_{\mathrm{h}}}{2}V_{\mathrm{eff}}\vec{\Psi}_y(\pm L,t) \\ &\quad - t'_{\mathrm{h}}S\vec{\Psi}_y(\pm L,t), \end{aligned} \tag{A7}$$

in which we define the matrix S by

$$S \equiv \begin{pmatrix}0&1\\1&0\end{pmatrix}. \tag{A8}$$

Thus, we can obtain the time-dependent Schrödinger equation in the *closed region* $|x| \le L$ as follows:

$$i\hbar\frac{\partial}{\partial t}\vec{\Psi}_y(x,t) = \begin{cases} -\frac{t_{\mathrm{h}}}{2}\{\vec{\Psi}_y[\pm(L-1),t] + V_{\mathrm{eff}}\vec{\Psi}_y(\pm L,t)\} - t'_{\mathrm{h}}S\vec{\Psi}_y(\pm L,t) & \text{for } x = \pm L \\ -\frac{t_{\mathrm{h}}}{2}[\vec{\Psi}_y(x-1,t) + \vec{\Psi}_y(x+1,t)] - t'_{\mathrm{h}}S\vec{\Psi}_y(x,t) & \text{for } 1 \le |x| \le L-1 \\ -\frac{t_{\mathrm{h}}}{2}[\vec{\Psi}_y(-1,t) + \vec{\Psi}_y(1,t)] - t'_{\mathrm{h}}S\vec{\Psi}_y(0,t) + g\Psi_{\mathrm{d}}(t)\begin{pmatrix}1\\0\end{pmatrix} & \text{for } x = 0 \end{cases} \tag{A9}$$

and

$$i\hbar\frac{\partial}{\partial t}\Psi_{\mathrm{d}}(t) = E_{\mathrm{d}}\Psi_{\mathrm{d}}(t) + g\Psi(0,1;t). \tag{A10}$$

This is the method by which we have produced the time-evolution simulations presented in Fig. 18.

*stergar@physics.utexas.edu
†hnakamura@nifs.ac.jp
‡hatano@iis.u-tokyo.ac.jp
§petrosky@physics.utexas.edu

[1] H. Nakamura, N. Hatano, S. Garmon, and T. Petrosky, Phys. Rev. Lett. **99**, 210404 (2007).
[2] S. Tanaka, S. Garmon, and T. Petrosky, Phys. Rev. B **73**, 115340 (2006).
[3] L. van Hove, Phys. Rev. **89**, 1189 (1953).
[4] G. D. Mahan, *Many Particle Physics*, 2nd ed. (Plenum Press, New York, 1990), pp. 283–285.
[5] T. Petrosky, C.-O. Ting, and S. Garmon, Phys. Rev. Lett. **94**, 043601 (2005).
[6] S. Garmon, Ph.D. thesis, The University of Texas at Austin, 2007.
[7] J. von Neumann and E. Wigner, Phys. Z. **30**, 465 (1929).
[8] F. H. Stillinger and D. R. Herrick, Phys. Rev. A **11**, 446 (1975).
[9] B. Gazdy, Phys. Lett. A **61**, 89 (1977).
[10] L. Fonda and R. G. Newton, Ann. Phys. (N.Y.) **10**, 490 (1960).
[11] E. C. G. Sudarshan, in *Field Theory, Quantization and Statistical Physics*, edited by E. Tirapegui (Reidel, Dordrecht, 1981), pp. 237–245.

[12] H. Friedrich and D. Wintgen, Phys. Rev. A **31**, 3964 (1985).
[13] G. Ordonez and S. Kim, Phys. Rev. A **70**, 032702 (2004).
[14] G. Ordonez, K. Na, and S. Kim, Phys. Rev. A **73**, 022113 (2006).
[15] A. F. Sadreev, E. N. Bulgakov, and I. Rotter, Phys. Rev. B **73**, 235342 (2006).
[16] E. N. Bulgakov, K. N. Pichugin, A. F. Sadreev, and I. Rotter, JETP Lett. **84**, 430 (2006).
[17] I. Rotter and A. F. Sadreev, Phys. Rev. E **71**, 046204 (2005).
[18] I. Rotter, J. Phys. A: Math. Theor. **42**, 153001 (2009).
[19] S. Longhi, Eur. Phys. J. B **57**, 45 (2007).
[20] S. Tanaka, S. Garmon, G. Ordonez, and T. Petrosky, Phys. Rev. B **76**, 153308 (2007).
[21] The two studies of the BIC are connected in the following sense: suppose that we have a single infinite chain of quantum dots labeled by discrete x with $-\infty < x < \infty$ and two impurities located at the sites $x = \pm n$. This gives a symmetric potential such that any solutions can be divided into symmetric or antisymmetric functions (both symmetries include the BIC effect). Note that the antisymmetric functions must vanish at $x=0$. Now suppose instead that we have a semi-infinite chain with sites labeled $0 \leq x < \infty$ and a single impurity at $x=n$. If the system is reflected about the $x=0$ site, then it is equivalent to the infinite chain with two impurities. In this case, however, the solutions must vanish at $x=0$ due to the boundary conditions. Therefore, only the antisymmetric sector of the infinite chain can be realized in the semi-infinite chain. The previous problem is that studied in Refs. 6 and 20, while the latter is studied in Ref. 19. In this sense, the problem in Ref. 19 is included in the problem in Refs. 6 and 20.
[22] F. Capasso, C. Sirtori, J. Faist, D. L. Sivco, S.-N. G. Chu, and A. Y. Cho, Nature (London) **358**, 565 (1992).
[23] P. S. Deo and A. M. Jayannavar, Phys. Rev. B **50**, 11629 (1994).
[24] J. Kondo, Prog. Theor. Phys. **32**, 37 (1964).
[25] O. Újsághy and A. Zawadowski, J. Phys. Soc. Jpn. **74**, 80 (2005); see also the other articles in the special-topic section "Kondo effect—40 years after the discovery" in J. Phys. Soc. Jpn. **74**, 1 (2005).
[26] K. O. Friedrichs, Commun. Pure Appl. Math. **1**, 361 (1948).
[27] N. Hatano, H. Nakamura, K. Sasada, and T. Petrosky, Prog. Theor. Phys. **119**, 187 (2008).
[28] K. Sasada and N. Hatano, Physica E (Amsterdam) **29**, 609 (2005).
[29] K. Sasada, N. Hatano, and G. Ordonez, arXiv:0905.3953 (unpublished).
[30] S. Datta, *Electronic Transport in Mesoscopic Systems* (Cambridge University Press, Cambridge, 1995).
[31] T. Berggren, Nucl. Phys. A **109**, 265 (1968).
[32] T. Petrosky, I. Prigogine, and S. Tasaki, Physica A **173**, 175 (1991).
[33] I. Antoniou and I. Prigogine, Physica A **192**, 443 (1993).
[34] J. Humblet and L. Rosenfeld, Nucl. Phys. **26**, 529 (1961).
[35] H. M. Nussenzveig, Nucl. Phys. **11**, 499 (1959).
[36] Note that Eq. (25) represents the same Hamiltonian (shifted by the energy t_h') presented in the earlier publication (Ref. 2) on the single-channel quantum wire.
[37] Note that if we chose to obtain an expansion for the energy of QBIC state R2 (instead of Q2) we would focus our attention on the embedded band edge at $t_h - t_h'$ and in our discussion of the cause of the QBIC effect the band edges would play the opposite role, with E_+ giving the embedded band edge and E_- being the embedding band. We mention how to obtain the final result for state R2 in another endnote (Ref. 38).
[38] State R2 is also QBIC under the conditions $E_d \ll t_h - t_h'$. In this region we can obtain an expansion for the eigenvalue of R2 from Eq. (41) by replacing each energy parameter with its negative value according to $t_h \to -t_h$, $t_h' \to -t_h'$, and $E_d \to -E_d$. [Essentially, the real terms in Eq. (41) become negative, while the imaginary term is unchanged.].
[39] E. N. Economou, *Green's Functions in Quantum Physics*, 2nd ed. (Springer-Verlag, Berlin, 1983).
[40] G. Binnig, H. Rohrer, Ch. Gerber, and E. Weibel, Phys. Rev. Lett. **49**, 57 (1982).
[41] See, for example, J. Tersoff and N. D. Lang, in *Theory of Scanning Tunneling Microscopy in Methods of Experimental Physics*, Scanning Tunneling Microscopy Vol. 27, edited J. A. Stroscio and W. J. Kaiser (Academic Press, New York, 1993), pp. 1–29.